International Journal of Mechanical Sciences 272 (2024) 109279

Contents lists available at ScienceDirect

International Journal of Mechanical Sciences

journal homepage: www.elsevier.com/locate/ijmecsci

Asymptotic *ps*-FEM for nonlinear analysis of composite shells

C.A. Yan *, R. Vescovini

Dipartimento di Scienze e Tecnologie Aerospaziali, Politecnico di Milano, Via La Masa 34, 20156 Milano, Italy

ARTICLE INFO

Keywords:
Finite element procedures
Solution algorithms
Nonlinear shell analysis
Mesh superposition techniques
Asymptotic-numerical method
Advanced refinement techniques

ABSTRACT

Nonlinear shell analysis relies typically on Finite Element Methods (FEMs) and Iterative-Incremental Procedures (IIPs). These methodologies can become computationally expensive whenever high-fidelity meshes are required to capture very localized features or extremely nonlinear responses. Aim of this study is presenting a novel computational tool based on an efficient finite element formulation, the *ps*-FEM, and a rapid perturbation solution procedure, the Asymptotic-Numerical Method (ANM). The proposed approach adopts a polynomial space enrichment strategy, the *p*-refinement, and a mesh superposition technique, the *s*-refinement, to build numerical models with quasi-optimal accuracy-to-error ratios. The introduced asymptotic framework enhances the effectiveness of solving nonlinear problems compared to IIPs. A set of test cases and new benchmarks is presented to validate the tool and demonstrate its potential. The present results show that challenging problems involving bifurcations, jumps, snap-backs and anisotropy-induced localizations can be solved with excellent degree of accuracy and relatively small modeling/computational effort.

1. Introduction

Numerical methods for simulating nonlinear phenomena are of primary importance in different engineering fields. For instance, nonlinear analyses are essential in aerospace engineering for assessing the stability of thin-walled shell structures, such as in the case of load-carrying components of aircraft and space launchers. In this context, Finite Element (FE) methods and Iterative-Incremental Procedures (IIPs) are typically employed as computational tools.

In spite of great flexibility and effectiveness of such numerical procedures, they often require large computational resources due to the large number of Degrees Of Freedom (DOFs) associated with the FE discretization, and the number of operations required by the solution method. This computational burden can pose challenges in real-world engineering applications where efficiency is of paramount importance, especially for routine tasks such as sensitivity analysis, optimization and design.

Over the years, significant efforts have been devoted to enhancing the efficiency of FE methodologies. In the classical approach developed in the 60's, numerical accuracy was improved by reducing the element size while keeping the polynomial order fixed to a low value, the so-called *h*-refinement. Early FE softwares were based on this refinement procedure. Nowadays, more advanced and efficient techniques are available, such as the *p*- and *hp*-extensions [1,2]. These strategies combine high-order shape functions with an element-wise representation of the solution. Recent implementations of this idea in FE codes can be found in the *p*-version of the Finite Element Method (*p*-FEM) of [3], where a *p*-refinement is exploited for increasing numerical efficiency and solving locking-related phenomena. The Hierarchical Finite Element Method (HFEM) [4] employs a similar principle to effectively resolve smooth solution features, such as natural frequencies and vibration modes. In [5] a *hp*-version of the Finite Element Method (*hp*-FEM), which employs simultaneous mesh refinements and polynomial space enrichment, is presented to improve convergence rates. The concept of Isogeometric Analysis (IGA) introduced by [6] also exploits a combined *h*- and *p*-refinements by using high-order Non-Uniform Rational B-Splines (NURBS) functions for the geometry and solution representation.

Adaptive refinement techniques are crucial for efficient FE methods. Indeed, they are a useful mean to optimize computational resources and achieve the desired level of accuracy in specific sub-portions of the domain. The *p*-adaptive FEM implemented in [7] represents an example of such methodologies, where the interpolation order is changed in an element-by-element way over a fixed mesh. In [8–12] different *h*-adaptivity approaches are proposed to improve locally the solution accuracy and minimize the geometric discretization error. In these approaches, however, only the mesh is refined while the polynomial order of the elements is maintained constant. An integrated approach is presented in [13–16], where combined adaptable *p*- and *h*-refinements are performed using different a-posteriori *hp*-error estimators.

The major limitations of adaptable FE methods is represented by the inconvenience of cumbersome transition meshes, time-consuming

* Corresponding author.
E-mail address: chengangelo.yan@polimi.it (C.A. Yan).

https://doi.org/10.1016/j.ijmecsci.2024.109279
Received 19 January 2024; Received in revised form 28 March 2024; Accepted 9 April 2024
Available online 18 April 2024

smoothing processes, special element formulations and multi-point constraints. Discretization techniques based on mesh superposition have been proposed recently to avoid these implementation complexities. These approaches rely upon the concept of "refine-by-superposition" introduced by Mote [11] in the early 70's. The underlining idea is to couple a global discretization with a local one by superposition of two incompatible meshes. This coupling proved to be useful to facilitate the refinement procedure and reduce the total number of DOFs, with consequent advantages on the computational costs. Different applications in the context of structural mechanics can be found in the literature. A mesh superposition strategy is proposed in [17] for buckling analysis of delaminated composite plates where localized deformation modes are observed. In [18,19], multiscale problems are efficiently handled with numerical discretization based on a global/p-refined mesh, combined with a local/overlaid one. Applications to fracture problems are presented in [20–22], which illustrate the flexibility of having an overlaying mesh in studying crack growth. A dynamic damage model is developed in [23] based on a mesh superposition technique. This study shows how stress/strain concentrations can be effectively captured by coupling a local, fine-scale discretization over a global/large-scale one. In the work of [24], microstructure of composites are modeled with a mesh superposition method to carry out accurate microscopic stress analysis and efficient sensitivity studies.

In addition to the refinement strategy, a pivotal role to achieve computational efficiency is played by the solution procedure. Nonlinear FE models are generally solved via IIPs. These algorithms are implemented in most FE codes for their effectiveness in determining nonlinear solution branches. For years researchers have devoted efforts to enhance the performance of IIPs, for example through improved predictor–corrector techniques [25,26], step-adaptation algorithms [27], convergence accelerators [28], and the formulation of continuation strategies [29–31]. Still, these procedures require a relatively large number of matrix factorizations and backward/forward substitutions which are necessary to carry out the prediction and correction steps. Furthermore, the automatization of the solution process is not always robust, as experience-based tuning is often required to avoid breakdown of the analysis.

An alternative way to solve nonlinear problems is represented by perturbation methods [32]. Within these techniques, the solution is approximated analytically as an asymptotic series in an expansion parameter. Within this approach a complex nonlinear problem can be decomposed into a sequence of simpler linear ones. To the best of the authors' knowledge, Thompson and Walker [33] were the first to combine a perturbation approach with a FE code to address a nonlinear structural problem. However, their method could not overcome, at that time, the IIPs [34]. Limitations were due to difficulties in deriving the terms of the series and the finite Range Of Validity (ROV) of the solution. Significant efforts in this field are due to Noor [35], who tried to extend the ROV of the solution by using a perturbation method with a reduced-basis technique. However, his approach did not bring significant improvements in efficiency over classical IIPs. This was due to the high computational cost for assembling the reduced-order equations [36]. This observation can partially explain why successive applications of perturbation techniques have been restricted to simple expansion series with few terms, typically the first two, to achieve qualitative approximations of the nonlinear solution [37–43].

In the early 90's, Damil and Potier-Ferry [44] approached perturbation methods for FE analysis with a new perspective, providing new research contributions of paramount importance in this field. The authors introduced a number of innovations that allowed perturbation and FE approaches to be combined very efficiently. A first contribution regards the introduction of a convenient formalism to ease and generalize the expansion procedure [45]. Furthermore, they extended the domain of validity of the method with Padè approximants [46]. Then, they proposed a perturbation method within a continuation algorithm to follow generic solution branches with minimum user tuning [47]. Their approach, today known in the literature as Asymptotic-Numerical Methods (ANMs) [48], has been successfully employed for solving a large variety of nonlinear shell problems, including post-buckling [49], bifurcation [50], nonlinear bending [51], large rotations [52], transient [53] and vibrations analysis [54,55]. More recently, ANMs have been applied to investigate free vibrations of perforated panels [56], forced vibration of visco-elastic structures [57,58], post-buckling of sandwich plates [59] and strips under stress [60], and optimization of Variable-Stiffness laminates [61]. All these studies and applications of ANMs demonstrated an improved efficiency and robustness of the solution process compared with traditional IIPs.

Motivated by these advancements, this paper aims to consolidate recent progress in numerical and analytical methods. Past efforts mainly focused on the independent improvement of FE schemes and perturbation procedures. We propose an integrated approach to achieve a unified numerical-asymptotic framework. Specifically, we propose an efficient FE technique based on mesh superposition, called the *ps*-version of the Finite Element Method (*ps*-FEM) [62], and the most state-of-the-art perturbation procedures, represented by the ANMs [48]. The result is an effective computational tool, where the numerical discretization can be tailored to the specific problem at hand, so that exceptionally high ratios between accuracy and size of the FE model are achieved. Moreover, the nonlinear solution paths are traced analytically in an accurate, efficient and fully automatic way by application of a perturbation procedure. To the best of the authors' knowledge, numerical schemes with the above mentioned capabilities cannot be found in the literature.

The manuscript is organized as follows: Section 2 presents the theoretical framework which is derived with the Hellinger–Reissner mixed variational principle. Section 3 shows the derivation of the expansion procedure for ANMs. Section 4 aims at illustrating the finite element approximation via *ps*-FEM approach and its integration with ANMs. In Section 5, test cases and new benchmarks are proposed to validate the present framework, demonstrate its potential and furnishing new results for future studies. The conclusion of this work are summarized in Section 6.

2. Theoretical framework

For generality, the governing equations are developed considering a three-dimensional continuum. This enables to derive a general set of equations which can be specified to structural theories in a subsequent step. First-order Shear Deformation Theory (FSDT) is considered here. For the sake of conciseness, the equations of shell theory are reported in Appendix.

By denoting the displacement field as $\mathbf{u}$, the Green–Lagrange strain tensor and its variation are given by

$$\mathbf{E} = \mathbf{E}_1(\mathbf{u}) + \frac{1}{2}\mathbf{E}_2(\mathbf{u}) \quad \text{and} \quad \delta\mathbf{E} = \mathbf{E}_1(\delta\mathbf{u}) + \mathbf{E}_{11}(\delta\mathbf{u}, \mathbf{u}), \tag{1}$$

where the strain operators $\mathbf{E}_1(\cdot)$, $\mathbf{E}_2(\cdot)$ and $\mathbf{E}_{11}(\cdot)$ are defined according to the mathematical model employed. The corresponding second Piola–Kirchhoff stress tensor $\mathbf{S}$ is related to the strains by a linear hyperelastic constitutive law

$$\mathbf{S} = \mathbb{C} : \mathbf{E}, \tag{2}$$

with $\mathbb{C}$ denoting the elasticity tensor.

The governing equations are obtained starting from the mixed Hellinger–Reissner functional

$$\Pi^*(\mathbf{u}, \mathbf{S}) = \int_\Omega \left(\mathbf{S} : \mathbf{E} - \frac{1}{2}\mathbf{S} : \mathbb{C}^{-1} : \mathbf{S} \right) \mathrm{d}\Omega - \int_\Omega \mathbf{u} \cdot \mathbf{b} \mathrm{d}\Omega - \int_\Gamma \mathbf{u} \cdot \mathbf{t} \mathrm{d}\Gamma, \tag{3}$$

which is written for a generic elastic body occupying a volume Ω bounded by Γ, and subjected to body pressures $\mathbf{b}$ and surface traction $\mathbf{t}$.

The mixed functional in Eq. (3) is a cubic function of the vector of unknowns $\mathbf{U} = \{\mathbf{u}, \mathbf{S}\}^{\mathrm{T}}$ due to the quadratic dependency of $\mathbf{E}$ to $\mathbf{u}$, see Eq. (1). Therefore, its variation yields a set of quadratic equations

$$\delta\Pi^*(\mathbf{u},\mathbf{S}) = \int_\Omega \left[\delta\mathbf{E} : \mathbf{S} + \delta\mathbf{S} : (\mathbf{E} - \mathbb{C}^{-1} : \mathbf{S})\right] \mathrm{d}\Omega - \int_\Omega \delta\mathbf{u}\cdot\mathbf{b}\mathrm{d}\Omega - \int_\Gamma \delta\mathbf{u}\cdot\mathbf{t}\mathrm{d}\Gamma = 0. \tag{4}$$

These equations correspond to the equilibrium condition and the constitutive law

$$\begin{cases} \int_\Omega \delta\mathbf{E} : \mathbf{S}\mathrm{d}\Omega = \int_\Omega \delta\mathbf{u}\cdot\mathbf{b}\mathrm{d}\Omega + \int_\Gamma \delta\mathbf{u}\cdot\mathbf{t}\mathrm{d}\Gamma \\ \mathbf{S} = \mathbb{C} : \mathbf{E}, \end{cases} \tag{5}$$

which are obtained by collecting the variations in $\delta\mathbf{u}$ and $\delta\mathbf{S}$ from Eq. (4), respectively.

For convenience, Eq. (4) is written in an operational form

$$L(\mathbf{U}) + Q(\mathbf{U},\mathbf{U}) - \lambda F = 0, \tag{6}$$

where λ is a loading parameter, while $L(\cdot)$, $Q(\cdot,\cdot)$ and F are mixed linear, quadratic and constant operators defined in Appendix.

The use of a mixed formulation permits more tractable equations to be obtained compared to a conventional displacement one, where additional cubic nonlinear terms would arise. This will provide a significant simplification in the derivation of the asymptotic expansions for ANMs.

3. Asymptotic expansions

The mixed nonlinear problem in Eq. (6) is solved via perturbation approach. To this purpose, three asymptotic approximations are developed, i.e. power, rational and piece-wise. Each of them provide a different analytical representation of the solution path, and can be coupled with a FE approximation to obtain different Asymptotic-Numerical Methods (ANMs). In this section, the derivation of the asymptotic expansions is done in a continuous/variational context. The solution of these expansions is achieved using a FE approach, discussed in Section 4.

3.1. Power approximation

The solution path $(\mathbf{U},\lambda)$ around the initial point $(\mathbf{U}_0,\lambda_0)$ can be approximated in terms of a truncated power series of the vector of unknowns and load factor [46],

$$\begin{aligned} &\mathbf{U} = \mathbf{U}_0 + \xi\mathbf{U}_1 + \xi^2\mathbf{U}_2 + \cdots + \xi^n\mathbf{U}_n \quad \text{and} \\ &\lambda = \lambda_0 + \xi\lambda_1 + \xi^2\lambda_2 + \cdots + \xi^n\lambda_n, \end{aligned} \tag{7}$$

where ξ is a perturbation parameter, while n is the order of truncation of the asymptotic expansion. By introducing Eq. (7) into Eq. (6) and equating power-like terms of ξ^k, a set of n linear mixed problems is obtained

$$\begin{aligned} k=1: &\quad T(\mathbf{U}_1) = \lambda_1 F, \\ k=n: &\quad T(\mathbf{U}_n) = \lambda_n F - \sum_{r=1}^{n-1} Q(\mathbf{U}_r,\mathbf{U}_{n-r}), \end{aligned} \tag{8}$$

where $T(\cdot) = L(\cdot) + Q(\mathbf{U}_0,\cdot) + Q(\cdot,\mathbf{U}_0)$ is the tangent stiffness operator evaluated at the initial point.

The system of Eq. (8) represents a sequence of linear non-homogeneous problems sharing the same stiffness operator. For each problem, the forcing term, i.e. the Right-Hand Side (RHS) of Eq. (8), depends on the load coefficient λ_k and the fields available from the solution of the lower order problems $\{\mathbf{U}_{k-1},\mathbf{U}_{k-2},\dots,\mathbf{U}_1\}^{\mathrm{T}}$.

To make the expansion of Eq. (7) unique, the following definition of the perturbation parameter ξ is introduced [46]

$$\xi = \frac{1}{a^2}\left[(\mathbf{U}-\mathbf{U}_0)\cdot\mathbf{U}_1 + (\lambda-\lambda_0)\lambda_1\right], \tag{9}$$

where the dot stands for the scalar product, while a is a scaling parameter corresponding to the length of the tangent vector $(\mathbf{U}_1,\lambda_1)$. A direct substitution of Eq. (7) into Eq. (9) leads to the conditions

$$\begin{aligned} k=1: &\quad \mathbf{U}_1\cdot\mathbf{U}_1 + \lambda_1\lambda_1 = 1, \\ k=n: &\quad \mathbf{U}_1\cdot\mathbf{U}_n + \lambda_1\lambda_n = 0. \end{aligned} \tag{10}$$

The power series in Eq. (7) is completely defined after solving Eq. (8) with Eq. (10). Following the approach presented in Ref. [46], the solution is achieved in two steps:

- Step 1: Change the formulation from mixed to displacement-based.
- Step 2: Introduce the numerical discretization.

The change of formulation is achieved through the introduction of the constitutive law described by Eq. (2) into Eqs. (8) and (10). This passage is detailed in the Appendix. The numerical approximation is performed using advanced displacement-based finite elements, as discussed in Section 4.

3.2. Rational approximation

Rational series tend to better approximate a function near a specific point than power series do [63]. Based on this consideration, the power representation of Eq. (7) can be transformed into an equivalent rational one based on Padé approximants [64],

$$\begin{aligned} &\mathbf{U} = \mathbf{U}_0 + r_1(\xi)\mathbf{U}_1 + r_2(\xi)\mathbf{U}_2 + \cdots + r_n(\xi)\mathbf{U}_n \quad \text{and} \\ &\lambda = \lambda_0 + r_1(\xi)\lambda_1 + r_2(\xi)\lambda_2 + \cdots + r_n(\xi)\lambda_n, \end{aligned} \tag{11}$$

where $r_k(\xi)$ are rational functions of order k dependent on the perturbation parameter ξ. In this work, they are constructed using the approach developed by Najah et al. [51],

$$r_i(\xi) = \left\{ \xi\frac{\Delta_{(n-2)}}{\Delta_{(n-1)}},\quad \xi^2\frac{\Delta_{(n-3)}}{\Delta_{(n-1)}},\quad \dots\quad ,\quad \xi^{n-1}\frac{1}{\Delta_{(n-1)}},\quad 0 \right\},\quad \text{for}\quad i=1,2,\dots,n, \tag{12}$$

where $\Delta_{(i)} = 1+\xi d_1+\xi^2 d_2+\cdots+\xi^i d_i$ are polynomials of order i dependent on

$$d_1 = -\frac{\alpha_{(n)(n-1)}}{\alpha_{(n-1)(n-1)}},\quad d_i = -\frac{\alpha_{(n)(n-i)}}{\alpha_{(n-i)(n-i)}} - \sum_{j=1}^{i-1}\frac{\alpha_{(n-j)(n-i)}}{\alpha_{(n-i)(n-i)}}d_j \quad \text{for}\quad i \le n-1, \tag{13}$$

while the scalar coefficients $\alpha_{(i)(j)}$ are obtained from a Gram–Schmidt orthogonization of the vector fields $\{\mathbf{U}_1,\mathbf{U}_2,\dots\mathbf{U}_n\}^{\mathrm{T}}$.

The rational representation above offers an advantage with respect to others presented in the past [64]. In particular, the expressions of Eq. (12) share the same denominator $\Delta_{(n-1)}$, hence reducing the number of poles that make the expansion singular in some points.

3.3. Piece-wise approximation

The truncated series in Eqs. (7) and (11) provide a local representations of the exact solution with a Range Of Validity (ROV) in the neighborhood of the initial point, i.e. $0 < \xi < \xi_{\mathrm{ROV}}$. To overcome this restriction, a piece-wise approximation can be employed [47]. The main idea consists in writing successive expansions

$$\begin{aligned} l=1: &\quad \mathbf{U} = \mathbf{U}_0^{(1)} + \sum_{k=1}^{n}\xi^k\mathbf{U}_k^{(1)} \quad \text{and} \quad \lambda = \lambda_0^{(1)} + \sum_{k=1}^{n}\xi^k\lambda_k^{(1)} \text{for} \quad 0<\xi<\xi_{\mathrm{ROV}}^{(1)} \\ l=j: &\quad \mathbf{U} = \mathbf{U}_0^{(j)} + \sum_{k=1}^{n}\xi^k\mathbf{U}_k^{(j)} \quad \text{and} \quad \lambda = \lambda_0^{(j)} + \sum_{k=1}^{n}\xi^k\lambda_k^{(j)} \text{for} \quad 0<\xi<\xi_{\mathrm{ROV}}^{(j)}, \end{aligned} \tag{14}$$

where the starting points $(\mathbf{U}_0^{(j)}\lambda_0^{(j)})$ of each series fall inside the ROV of the previous one $0 < \xi < \xi_{\mathrm{ROV}}^{(j-1)}$.

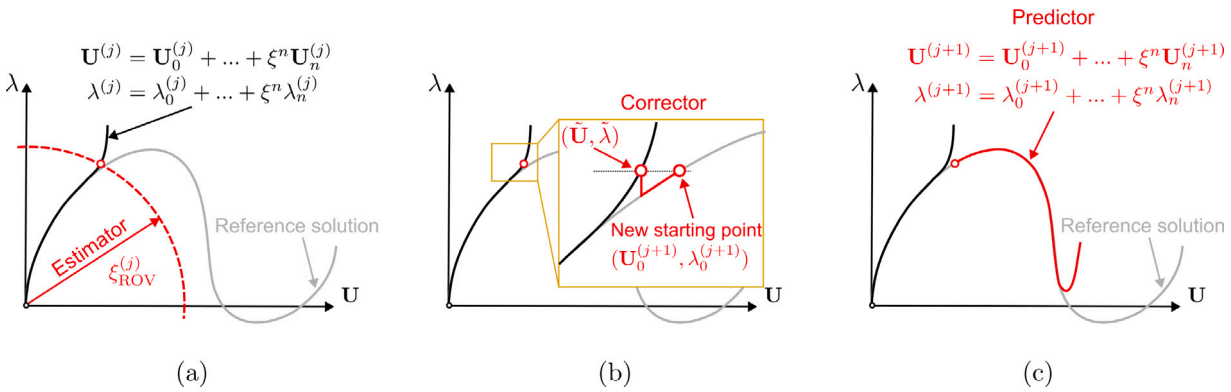

Fig. 1. Building blocks of the continuation algorithm: (a) estimator, (b) corrector and (c) predictor. The ANM performs different estimation, correction and prediction steps to generate an analytical piece-wise representation of the solution path: in the estimation phase the radius of validity of the predictor is determined, in the correction phase the starting point of the predictor is corrected, in the prediction phase a new series expansion is generated to approximate the solution path.

In the present work, this concept is implemented with a continuation algorithm which employs a predictor, an estimator and a corrector. A graphical representation of the workflow is presented in Fig. 1. The three different building blocks are discussed in the following.

Predictor

In the predictor phase, a perturbation method is employed to solve the problem around a starting point $(\mathbf{U}_0^{(j)}, \lambda_0^{(j)})$. In the developed continuation algorithm, the predicted solution is expressed in the form of a power series

$$\begin{aligned} &\mathbf{U} = \mathbf{U}_0^{(j)} + \xi \mathbf{U}_1^{(j)} + \xi^2 \mathbf{U}_2^{(j)} + \cdots + \xi^n \mathbf{U}_n^{(j)} \quad \text{and} \\ &\lambda = \lambda_0^{(j)} + \xi \lambda_1^{(j)} + \xi^2 \lambda_2^{(j)} + \cdots + \xi^n \lambda_n^{(j)}, \end{aligned} \tag{15}$$

where the superscript j identifies the prediction step.

Power representation is preferred over rational ones due to better analytic properties. Indeed, power series do not suffer from the presence of poles, which is desirable to guarantee robustness in the continuation algorithm.

Estimator

An estimator is used to calculate the ROV of the series in Eq. (15) and define the starting point for the subsequent prediction step $(\mathbf{U}_0^{(j+1)}, \lambda_0^{(j+1)})$. The ROV is computed using the criterion introduced by Cochelin [47]

$$\xi_{\text{ROV}}^{(j)} = \left(\epsilon \frac{\mathbf{U}_1^{(j)}}{\mathbf{U}_n^{(j)}} \right)^{\frac{1}{(n-1)}}, \tag{16}$$

where ϵ is a scalar which defines the accuracy criteria.

The definition of the ROV in Eq. (16) is based on the following empirical observation: the terms in the perturbation expansion tend to be similar inside the ROV of the series, while they separate quickly when this radius is reached. Hence, the ratio between the first $\mathbf{U}_1$ and last terms $\mathbf{U}_n$ of the series can be used to check whether the ROV is reached or not. This simple criterion provides a good approximation of the ROV of the solution, while requiring almost no additional computational cost.

Corrector

The corrector phase is introduced to bound the error while progressing along the solution path. This is achieved by correcting the starting points before the beginning of each prediction step. Assuming $(\tilde{\mathbf{U}}, \tilde{\lambda})$ to be a trial solution of Eq. (6) at the end of the prediction step j, i.e. Eq. (15) evaluated at Eq. (16), the correction is performed by standard Newton–Raphson iterations

$$\begin{aligned} &\mathbf{U}_{(i+1)} = \mathbf{U}_{(i)} + \Delta\mathbf{U}, \qquad \text{with} \quad \mathbf{U}_{(0)} = \tilde{\mathbf{U}}, \\ &T(\Delta\mathbf{U}) = -R(\mathbf{U}_{(i)}, \tilde{\lambda}), \end{aligned} \tag{17}$$

where $R(\cdot, \lambda) = L(\cdot) + Q(\cdot, \cdot) - \lambda F$ is the residual operator, while the subscript i is the iteration index. The process is repeated until the norm of the residual is below a pre-defined tolerance.

4. Finite element approximation

This work adopts an advanced spatial discretization based on the *ps*-version of the Finite Element Method (*ps*-FEM) [62]. In the following, the main features of this FE approach are recalled with reference to the polynomial space construction, the mesh design and the refinement procedure. Finally, the so-obtained FE scheme is employed to compute the asymptotic terms derived in Section 3.

4.1. Polynomial space construction

The polynomial space S^p is constructed from the set of one-dimensional hierarchical functions introduced by Babuška et al. [1] and applied in the *p*-FEM

$$\begin{aligned} &f_1(\eta) = \frac{1}{2}(1+\eta), \quad f_2(\eta) = \frac{1}{2}(1-\eta), \\ &f_{k+1}(\eta) = \sqrt{\frac{2k-1}{2}} \int_{-1}^{\eta} P_{k-1}(\eta')\mathrm{d}\eta', \quad \text{for} \quad k = 2, 3, \ldots, p, \end{aligned} \tag{18}$$

where

$$\begin{aligned} &P_0(\eta) = 1, \quad P_1(\eta) = \eta \\ &P_k(\eta) = \frac{1}{k}\left[\eta(2k-1)P_{k-1}(\eta) - (k-1)P_{k-2}(\eta)\right], \quad \text{for} \quad k = 2, 3, \ldots, p, \end{aligned} \tag{19}$$

are Legendre polynomial functions of order k. The functions belonging to this series expansion can be divided into two categories, i.e. nodal and internal mode functions. The former are the well-known Lagrange linear interpolation polynomials, $f_1(\eta)$ and $f_2(\eta)$, while the latter are represented by the higher-order terms $f_k(\eta)$ (with $k > 2$) based on the integrals of Legendre polynomials. The combination of nodal and internal mode functions leads to different types of two-dimensional shape functions, i.e., nodal (two nodal modes), edge (one nodal mode and one internal mode), and face (two internal modes) shape functions. A graphical illustration is reported in Fig. 2.

The functions depicted in Fig. 2 form a quasi-orthogonal and hierarchical polynomial space. These properties give two major advantages in the numerical computations. Firstly, the resulting tangent stiffness matrix $\mathbf{T}$ is well-conditioned even for very high polynomial orders p. Secondly, the refinement of the series (or *p*-refinement) can be performed easily, with no need to reassemble all the FE system.

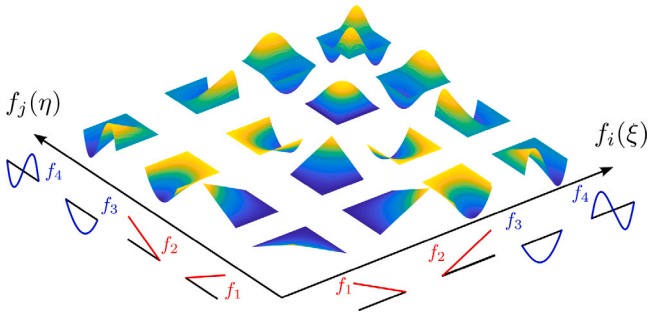

Fig. 2. Polynomial space employed in the *ps*-FEM. Three families of two-dimensional shape functions form the polynomial space: nodal, edge and face functions. Nodal functions are non-zero at only one node. Edge functions are non-zero at only one edge. Face functions are zero on all four nodes and edges.

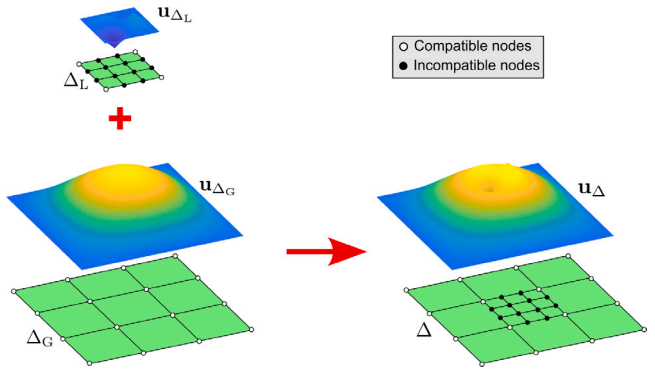

Fig. 3. Mesh design by "refine-by-superposition". A coarse/global mesh Δ_G is overlapped by a fine-scale/local one Δ_L. The final numerical solution is given by the sum of the global and local discretizations, $\mathbf{u}_{\Delta_G}$ and $\mathbf{u}_{\Delta_L}$, respectively, and by the imposition of proper compatibility and linear independence conditions on the shape functions [67].

4.2. Mesh design

The finite element mesh – denoted here with the letter Δ – is constructed using the concept of solution superposition, first introduced by Mote [65] and later implemented in the *s*-FEM [66]. The idea is to decompose the FE approximation $\mathbf{u}_\Delta$ into global and local parts, $\mathbf{u}_{\Delta_G}$ and $\mathbf{u}_{\Delta_L}$, through a mesh superposition technique

$$\mathbf{u} \simeq \mathbf{u}_\Delta = \begin{cases} \mathbf{u}_{\Delta_G} & \text{in} \quad \Omega - \Omega_L \\ \mathbf{u}_{\Delta_G} + \mathbf{u}_{\Delta_L} & \text{in} \quad \Omega_L, \end{cases} \tag{20}$$

where Ω is the computational domain discretized by the global mesh Δ_G, while Ω_L is the region of superposition, where a local/finer mesh Δ_L is defined , see Fig. 3.

The possibility of decomposing the solution as outlined above is subjected to two requirements: the compatibility of the basis functions and their linear independence. The former condition is ensured by imposing homogeneous Dirichlet boundary conditions on the boundary of the local mesh. The latter is enforced by "deactivating" redundant nodal, side and face shape functions operating on the same mesh region [67].

The main advantage of this approach relies on the possibility of reducing the element size h at local level. It follows that local mesh refinements can be carried out without the need of employing transition elements or enforcing multi-point constraint conditions [68,69].

4.3. Refinement procedure

In the *ps*-FEM, the refinement process is taken from Zander [21], and is outlined in Fig. 4.

In the first step, the global mesh Δ_G is defined. Its resolution h is chosen to guarantee a correct imposition of the boundary/loading conditions and avoid the introduction of excessively distorted elements to represent the problems' geometry. The interpolation order of the elements, p, is increased until the desired accuracy is reached at global level.

In the second step, a local mesh Δ_L is generated and superimposed to the global one. This operation is performed for any region where a local response is of concern. In particular, the procedure to construct Δ_L is illustrated in Fig. 5.

Firstly, the region of local refinement is chosen and the elements belonging to this region are divided into four parts. Then, the resulting sub-elements are used to define the superimposing mesh. To further decrease the elements size h, different layers of local meshes can be generated and superimposed one over the others. This recursive procedure can be done following an isotropic subdivision of the elements ($q = 0$) or a more general anisotropic subdivision ($q > 0$).

The availability of a *p*- and *s*-extension allows for various *ps*-refinement strategies to be implemented [21]. By proper adjustment of the elements' order and size in accordance with the smoothness characteristics of the solution, improved trade-off between accuracy and computational cost are reached compared with conventional FE approaches. In general, global quantities (gross displacements, natural frequencies, buckling loads) can be effectively captured with a combination of coarse and high-order elements. On the other hand, local features (stress concentrations, solution gradients, singularity points) are accurately represented by adding a local mesh combining small and lower-order elements.

4.4. Computation of asymptotic terms

The discrete asymptotic equations are obtained by elaborating the pseudo-mixed set of Eqs. (8) and (10) with the steps presented in Appendix. The resulting set of equations is

$$\begin{aligned} k = 1: \quad & \mathbf{T}\mathbf{c}_1 = \lambda_1 \mathbf{f} \quad \text{and} \quad \mathbf{c}_1{}^{\mathrm{T}}\mathbf{c}_1 + \lambda_1\lambda_1 = 1, \\ k = n: \quad & \mathbf{T}\mathbf{c}_n = \lambda_n \mathbf{f} - \mathbf{q}_n \quad \text{and} \quad \mathbf{c}_n{}^{\mathrm{T}}\mathbf{c}_1 + \lambda_n\lambda_1 = 0, \end{aligned} \tag{21}$$

where $\mathbf{T}$ is the tangent stiffness matrix, $\mathbf{f}$ is the vector of the external forces, while $\mathbf{q}_k$ is the vector of the nonlinear terms; the vector $\mathbf{c}_k$ denotes the numerical solution of the kth order problem, whose evaluation is carried out as

$$\begin{aligned} & \hat{\mathbf{c}}_1 = \mathbf{T}^{-1}\mathbf{f}, \qquad \lambda_1 = \frac{1}{\sqrt{1 + \hat{\mathbf{c}}_1{}^{\mathrm{T}}\hat{\mathbf{c}}_1}}, \qquad \mathbf{c}_1 = \lambda_1 \hat{\mathbf{c}}_1, \\ & \hat{\mathbf{c}}_k = \mathbf{T}^{-1}\mathbf{q}_k, \quad \lambda_k = -\frac{\mathbf{c}_1{}^{\mathrm{T}}\hat{\mathbf{c}}_k}{a^2}\lambda_1, \qquad \mathbf{c}_k = \frac{\lambda_k}{\lambda_1}\mathbf{c}_1 + \hat{\mathbf{c}}_k \quad \text{for} \quad k > 1. \end{aligned} \tag{22}$$

Note, one single factorization of the tangent stiffness matrix $\mathbf{T}$ is needed. Furthermore, it is noted that the number of operations to construct the nonlinear vectors $\mathbf{q}_k$ is similar to the evaluations of the residual vector $\mathbf{r}$. Once the vectors of unknowns $\mathbf{c}_k$ are available, the final FE solution is

$$\mathbf{c} = \mathbf{c}_0 + \xi\mathbf{c}_1 + \xi^2\mathbf{c}_2 + \cdots + \xi^n\mathbf{c}_n. \tag{23}$$

5. Results

The numerical-asymptotic framework is now applied to the analysis of composite plates and shells. Aim of this section is to illustrate the potential of the proposed approach, relying on the combination of an efficient numerical method (*ps*-FEM) and a fast solution procedure (ANM).

In the following, different challenging test cases are proposed. Whenever available, comparison is done with literature results. In all other cases, Abaqus is used to generate reference solutions. For the sake of clarity, the nomenclature used for the FE models is explained in Table 1.

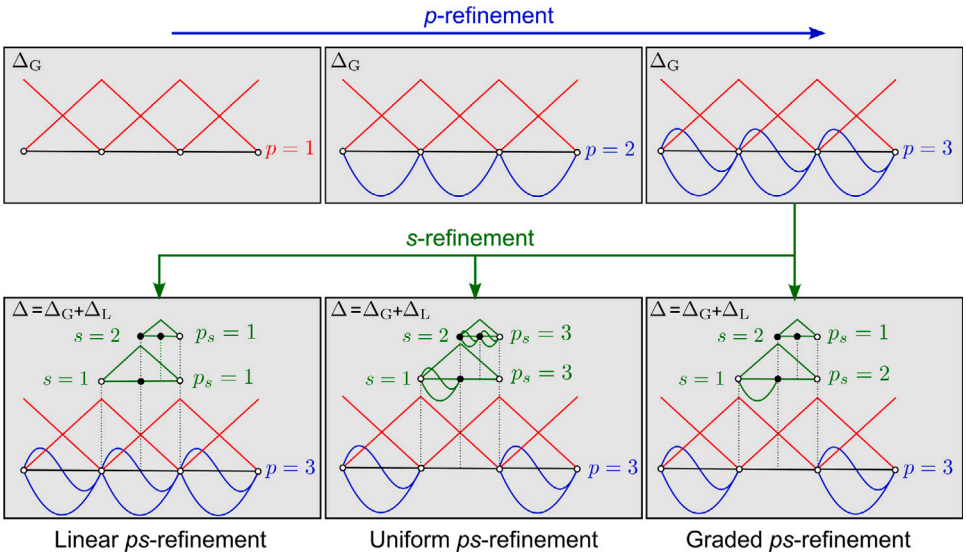

Fig. 4. Refinement procedures implemented in the *ps*-FEM. The *p*- and *s*-refinement are combined to have different *ps*-refinement strategies. In the linear *ps*-refinement, *p*-refinement is performed only on the global mesh, while multi-level *s*-refinements are carried out with linear elements. In the uniform *ps*-refinement, *p*-refinement is performed uniformly on global and local meshes, such that all elements have the same order *p*. In the graded *ps*-refinement, *p*-refinement is performed independently on global and local meshes.

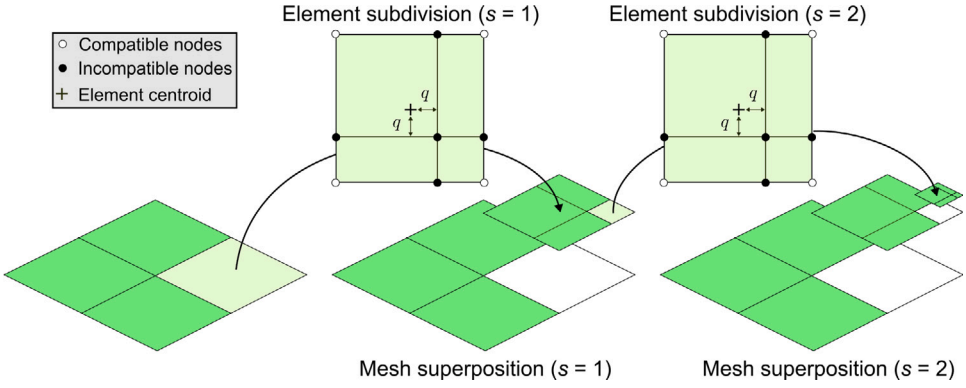

Fig. 5. Mesh refinement procedure implemented in the *ps*-FEM: (1) Elements in the region of refinement are quartered with an isotropic ($q = 0$) or anisotropic ($q > 0$) subdivision rule, (2) an incompatible local mesh is generated from the resulting sub-elements and superimposed to the underlying mesh, (3) the process is repeated until a desired resolution h is reached.

Table 1
Nomenclature for the FE models.

FE model	Element formulation	Refinement strategy	Solution algorithm
h-Model[a]	Lagrange elements	*h*-refinement	Iterative-Incremental
p-Model	Hierarchical elements	*p*-refinement	Asymptotic-Numerical
ps-Model	Hierarchical elements	*ps*-refinement	Asymptotic-Numerical

[a] Generated with Abaqus using S4R elements.

For instance, when an *h*-Model is used, the type of element, the refinement and the solution strategies are specified based on the information presented in the table. In addition, a summary of the features of the FE models used in this section is available in Table 2.

For each test case, information is provided regarding the number of elements, the order of polynomial interpolation and the number of overlaid meshes, the latter equal to zero whenever no local refinement is performed. The last column reports the total number of degrees of freedom, which is crucial for establishing the convenience of a refinement strategy with respect to another. Further details on the parameters of the solution procedures are provided in Table 3.

Test 1: Cylindrical roof

The first test case considers a hinged cylindrical roof loaded with a concentrated force. This benchmark problem is taken from Ref. [70], and is chosen for its complex nonlinear response, where several jumps phenomena are observed.

The problem is schematized in Fig. 6, where the following geometric parameters are considered: $L = 508$ mm, $R = 2540$ mm, $\theta = 0.1$ rad, $t = 6.35$ mm. The shell is made of composite material with mechanical properties given by $E_{11} = 3300$ GPa, $E_{22} = 1100$ GPa, $G_{12} = G_{13} = G_{23} = 660$ GPa, $\nu_{11} = 0.25$. A cross-ply lamination sequence [90/0/90] is considered.

Table 2
Features of the FE models.

	FE Model	Mesh Resolution (h)[a]	Polynomial Order (p)	Superposition Levels (s)	Degrees of Freedom
Test 1	*ps*-Model	2 × 2 elements	$p = 4$	$s = 4$	471
Test 2	*p*-Model	8 elements	$p = 5$	$s = 0$	1,054
Test 3	*p*-Model	4 × 20 elements	$p = 5$	$s = 0$	10,299
Benchmark 1	*h*-Model	20 × 20 elements	$p = 1$	$s = 0$	2,646
		40 × 40 elements	$p = 1$	$s = 0$	10,086
		100 × 100 elements	$p = 1$	$s = 0$	61,206
		200 × 200 elements	$p = 1$	$s = 0$	242,406
	p-Model	20 × 20 elements	$p = 2$	$s = 0$	8,019
		20 × 20 elements	$p = 3$	$s = 0$	18,019
		20 × 20 elements	$p = 4$	$s = 0$	32,019
	ps-Model	4 × 4 elements	$p = 6$	$s = 1$	3,483
		4 × 4 elements	$p = 6$	$s = 2$	3,843
		4 × 4 elements	$p = 6$	$s = 3$	4,023
Benchmark 2	*h*-Model	640 elements	$p = 1$	$s = 0$	4,230
		1,932 elements	$p = 1$	$s = 0$	12,270
		3,920 elements	$p = 1$	$s = 0$	24,486
		9,984 elements	$p = 1$	$s = 0$	61,406
		18,832 elements	$p = 1$	$s = 0$	115,110
	ps-Model	44 elements	$p = 3$	$s = 1$	2,406
		44 elements	$p = 4$	$s = 2$	5,092
		44 elements	$p = 5$	$s = 3$	9,318
Benchmark 3	*h*-Model	270 × 90 elements	$p = 1$	$s = 0$	147,420
	ps-Model	20 × 4 elements	$p = 5$	$s = 3$	11,179

[a] The format $a \times b$ is used whenever the mesh is uniform.

Table 3
Parameters of the solution algorithms.

	Algorithm	Representation	Predictor	Estimator	Corrector
Test 1	ANM	Power	$n = 10, 30, 50$	/	/
		Rational	$n = 10, 30, 50$	/	/
		Power piece-wise	$n = 10$	$\epsilon = 10^{-3}$	tol $= 10^{-7}$
Test 2	ANM	Power piece-wise	$n = 20$	$\epsilon = 10^{-5}$	tol $= 10^{-7}$
Test 3	ANM	Power piece-wise	$n = 15$	$\epsilon = 10^{-4}$	tol $= 10^{-7}$
Benchmark 1	ANM	Power piece-wise	$n = 10$	$\epsilon = 10^{-3}$	tol $= 10^{-7}$
	IIP[a]	Linear piece-wise	$n = 1$	/	tol $= 5 \times 10^{-3}$
Benchmark 2	ANM	Power piece-wise	$n = 15$	$\epsilon = 10^{-3}$	tol $= 10^{-7}$
	IIP[a]	Linear piece-wise	$n = 1$	/	tol $= 5 \times 10^{-3}$
Benchmark 3	ANM	Power piece-wise	$n = 10$	$\epsilon = 10^{-3}$	tol $= 10^{-7}$
	IIP[a]	Linear piece-wise	$n = 1$	/	tol $= 5 \times 10^{-3}$

[a] Riks method in Abaqus; IIP: Incremental-Iterative Procedure; ANM: Asymptotic-Numerical Method.

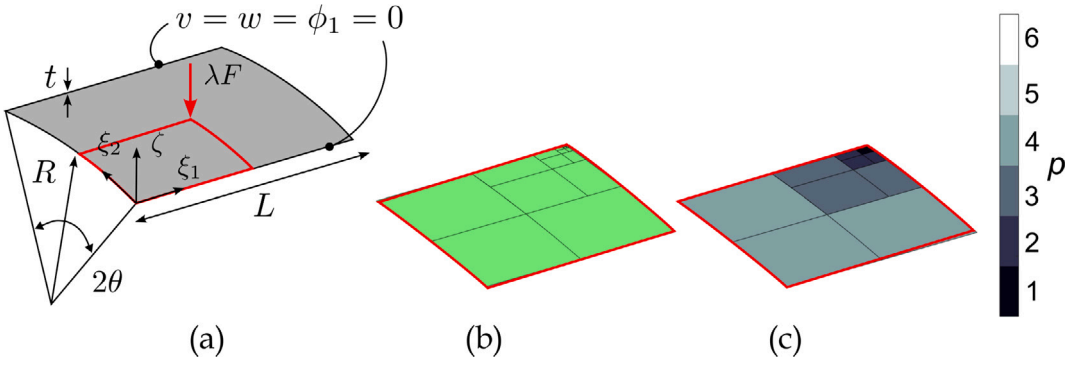

Fig. 6. Cylindrical roof problem. Geometric quantities are referred to the shell middle surface, while boundary conditions are defined in terms of middle displacement (u, v, w) and rotation (ϕ_1, ϕ_2) components in a curvilinear reference system (ξ_1, ξ_2, ζ). The finite element model is generated considering one quarter of the shell, and is defined in terms of mesh resolution h, and element polynomial order p.

The FE model is generated by exploiting the double symmetry of the problem, as illustrated in Fig. 6. Simulations are conducted with a mesh of 2 × 2 elements of order $p = 4$ and a local refinement at the point of application of the load. A total of $s = 4$ local meshes are superimposed in the context of a graded *ps*-refinement strategy. A linear grading rule is adopted for the construction of the FE model, where p_s and p are the polynomial degrees of the elements at the sth superposition level and at the base level ($s = 0$), respectively. The constant m is a tuning parameter, here taken equal to 1.

$$p_s = p - \text{floor}\left(\frac{s}{m}\right) \tag{24}$$

With the purpose of validating the solution procedures presented in Section 3, three different perturbation strategies are considered by adopting power, rational and power piece-wise series representations. The features of the solution algorithms are summarized in Table 3.

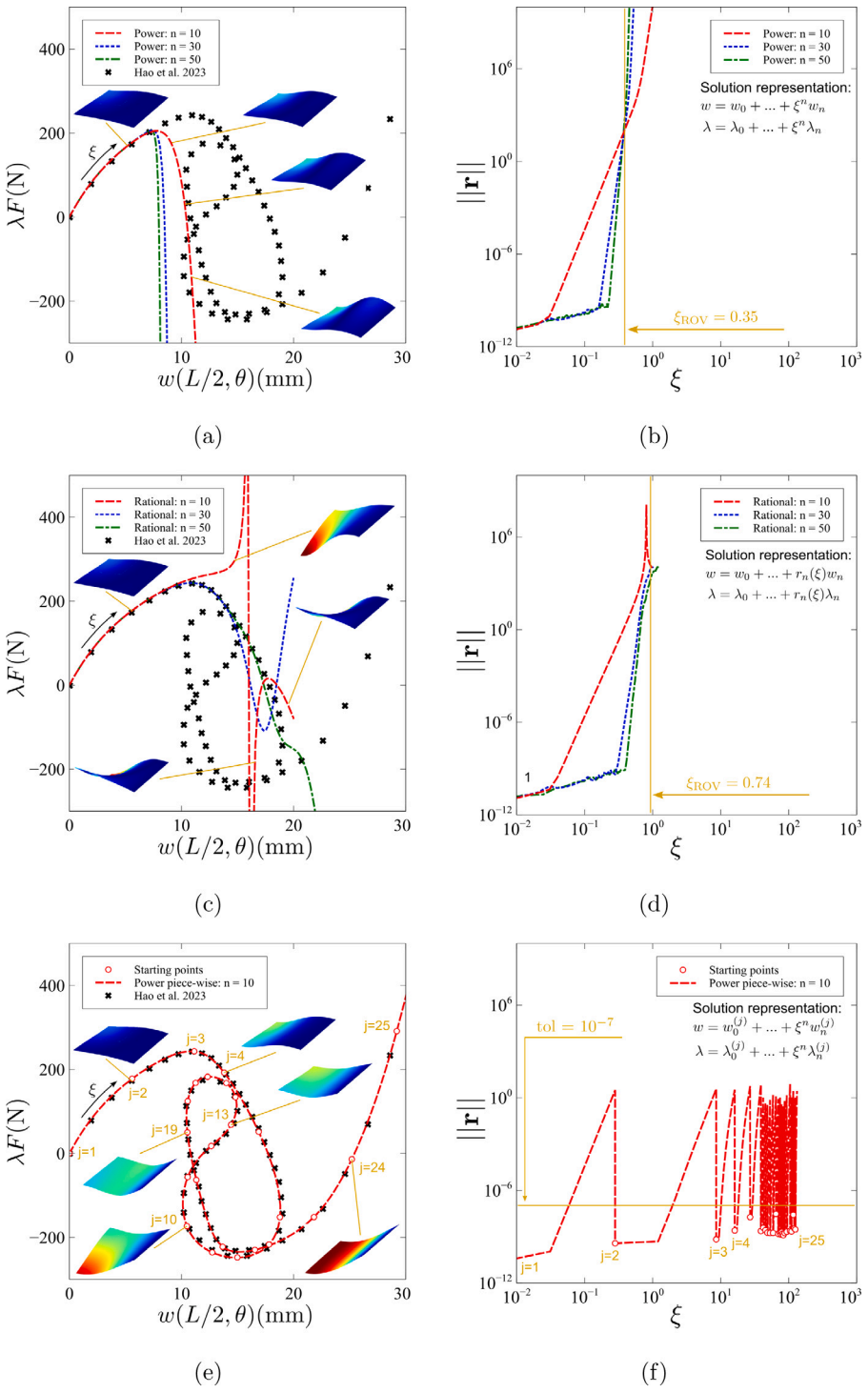

Fig. 7. Solution of the cylindrical roof problem. The first column reports load–deflection curves. The second column reports error curves. Rows refer to the curves obtained with different analytical representations: power (first row), rational (second row) and power piece-wise (third row). Deflection shapes are plotted with a magnification factor of 5, while contour colors are generated in terms of $\sqrt{u^2 + v^2 + w^2}$ and normalized with a factor of 25 mm.

The results of the analysis are illustrated in Fig. 7.

The comparison is presented in terms of load–deflection curves, see Figs. 7a, Figs. 7c and 7e, against the results reported by Hao et al. [70], where a NURBS-based FE method is adopted in conjunction with an IIP. Furthermore, the norm of the residuals is shown in Figs. 7b, 7d and 7f, for different values of the expansion parameter ξ.

From Fig. 7a, one can see that the power series solution is capable of representing a considerable branch of the solution. The path-length covered is equivalent to the one obtained with 4 – 5 incremental steps in Ref. [70], where a spherical arc-length method is used. For this problem, the Radius Of Validity (ROV) of the series is estimated to be $\xi_{\mathrm{ROV}} = 0.35$. Once this threshold is reached, the solution starts diverging, as clear from the analysis of the error in Fig. 7b.

The ROV of the solution can be drastically extended by referring to a rational representation, as illustrated in Fig. 7c. In this case, a single series is capable of covering the equivalent path obtained in the reference with 15 – 16 incremental steps. As seen, this corresponds to

Table 4
Comparison of Radius of Validity between different series representations — cylindrical roof.

Representation	Radius of validity
Power	$\xi_{\text{ROV}} = 0.35$
Rational	$\xi_{\text{ROV}} = 0.74$
Power piece-wise	$\xi_{\text{ROV}} = \infty$

more than double the range of the power expansion. The values are summarized in Table 4.

Despite these excellent performances, rational series are sensitive to the presence of poles [46], which can deteriorate the quality of the solution along the solution path. Poles may appear also inside the ROV, see the solution for $n = 10$ in Fig. 7c-7d. These drawbacks affect the robustness of the approach, unless special measures are taken to predict their appearance [49]. The limitation of the ROV can be eliminated by applying the ANM as an high-order predictor within a continuation procedure. This approach enables a piece-wise representation of the solution to be obtained, where each interval of the equilibrium path is represented with different expansion series.

The results of Fig. 7e are obtained using a power series predictor of order $n = 10$, a ROV estimator with a step control parameter $\epsilon = 10^{-3}$, and Newton–Raphson corrector with tolerance tol $= 10^{-7}$. As seen, the complete solution path can be obtained with 25 prediction steps. This represents a reduction of approximately $1/3$ the number of increments compared to the arc-length method of [70]. Furthermore, by introducing a correction step before the definition of each series the norm of the error cannot diverge, as clear from Fig. 7f: at every correction step the error is brought below the specified tolerance level, hence leading to the zig-zag response exhibited by the curve.

Due to the accuracy of the results, insights on the shell response can be gained. From Fig. 7e it can be seen that the shell buckles at a load level of about 243 N, which represents its ultimate bearing capability. This effect is not captured correctly by a simple power and rational series, see Figs. 7a and 7c, due to the limited ROV and/or the presence of poles. After the ultimate load, the solution follows an intricate path where several turning points are encountered, each of these with a very different deformation mode, see Fig. 7e. This complex behavior is due to the particular orthotropic lamination sequence considered and the high thinness of the shell [70].

The unrestricted ROV and the high robustness make the power piece-wise series the best solution approach among the ones presented in Section 3. For this reason, this strategy will be applied to solve the remaining set of test cases.

Test 2: Plate with circular cutout

The second test case regards a Variable-Stiffness (VS) plate with a cutout [71]. Aim of this section is demonstrating the validity of the proposed approach in the presence of complex geometries and material properties distributions.

The characteristics of the plate are presented in Fig. 8 along with its FE model. The plate is characterized by $L = 254$ mm, $D/L = 0.6$, $t = 2.0352$ mm.

The nominal geometry is altered by an initial imperfection with a shape corresponding to the first buckling mode and maximum amplitude equal to 1% of the thickness. The material properties are given by $E_{11} = 181,000$ MPa, $E_{22} = 10,273$ MPa, $G_{12} = G_{13} = G_{23} = 7,170.5$ MPa, $\nu_{12} = 0.28$, while the VS lamination sequence is defined by $[\pm 90\langle 0, 75\rangle]_{4s}$.

The plate is simply supported at the four sides, with out-of-plane deflections and torsional rotations set to zero. In addition, the loaded edges are free to translate, but forced to remain straight, this condition being imposed with a multi-point constraint. The load is introduced with a concentrated force applied to two reference nodes, one for each side, as illustrated in Fig. 8a.

The FE model is composed by 8 elements of order $p = 5$, as shown in Figs. 8b-8c. No local refinement is required despite the presence of a cutout. Indeed, the VS layup allows for a proper redistribution of stresses with a resulting mitigation of stress gradients [71].

The numerical solution is sought with a continuation strategy, whose parameters are available in Table 3. In particular, the predictor is a power series of order $n = 20$, the ROV estimator is specified to be $\epsilon = 10^{-5}$, and the tolerance of the corrector is fixed to 10^{-7}.

The results are presented in Fig. 9 through equilibrium and error curves. The equilibrium curves are expressed in terms of average edge resultant and strain,

$$\overline{N}_{11} = \frac{1}{L}\int_{-L/2}^{L/2} N_{11}(\pm L/2, \xi_2)d\xi_2 \quad \text{and} \quad \bar{\epsilon}_{11} = \frac{1}{L}\int_{-L/2}^{L/2} u(\pm L/2, \xi_2)d\xi_2, \tag{25}$$

which are normalized with respect to the critical buckling resultant $\overline{N}_{\text{c}}^{\text{iso}}$ and strain $\bar{\epsilon}_{\text{c}}^{\text{iso}}$ of a quasi-isotropic laminate without cutout. For the material properties considered, the corresponding equivalent Poisson's coefficient and Young modulus are $\nu_{\text{iso}} = 0.296$ and $E_{\text{iso}} = 69,668$ MPa [71].

The present results are compared with the ones of Li et al. [71], obtained with a Ritz method and IIP. From Fig. 9a one can see an excellent degree of agreement of the pre- and post-buckling equilibrium paths. For this plate problem, buckling occurs at an end-shortening level of about $5 \times \bar{\epsilon}_{\text{c}}^{\text{iso}}$. After the jump from the primary to secondary branch, the plate buckles with a single half-wave.

Besides the excellent quality of results, different considerations can be made in terms of choice of numerical method and solution procedure. In particular, the convergence analysis in [71] shows that the Ritz model requires 3,732 DOFs to converge. On the other hand, the present FE model employs only 1,054 DOFs. These savings demonstrate how a high-order/piece-wise approximation is more suitable than a high-order/element-free one in the presence of a complex geometry. Indeed, element-free approaches require special penalty factors to correctly describe a generic geometry. This often undermines the convergence performance of these methods due to ill-conditioning of the numerical matrices.

Regarding the solution procedure, the ANM requires only 5 prediction steps to trace the equilibrium curve. This represents less than 1/10 the number required by the IIP used in Ref. [71], where approximately $55 - 60$ incremental steps were needed. Considering that in the present approach the average number of corrections per step is only 2, see Fig. 9b, the reduction in computational time is noticeable.

The comparison in this section provides clear insights into the ability of the proposed strategy to handle the nonlinear response of VS structures. As seen, the combination of ANM and few high-order element allows to combine the inherent flexibility of FE procedures with the performance of Ritz-like approaches.

Test 3: Water's composite cylinder

The third test case deals with the Water's composite shell, which is a typical benchmark for numerical validation of shell problems [72,73]. The post-buckling analysis of axially loaded cylinders is a challenging task for nonlinear solution algorithms. Indeed, the presence of limit loads and sudden snap-backs requires special care, and have stimulated in the years the development of several ad-hoc solution procedures [29,31]. The present test case aims at verifying the robustness of the present FE-approach to the analysis of this challenging problem.

The cylinder under investigation and its FE discretization are shown in Fig. 10. The geometry is defined by $L = 355.6$ mm, $R = 203.19$ mm, and $t = 1.016$ mm. The lamination sequence is $[\pm 45/0/90]_{\text{s}}$, where the

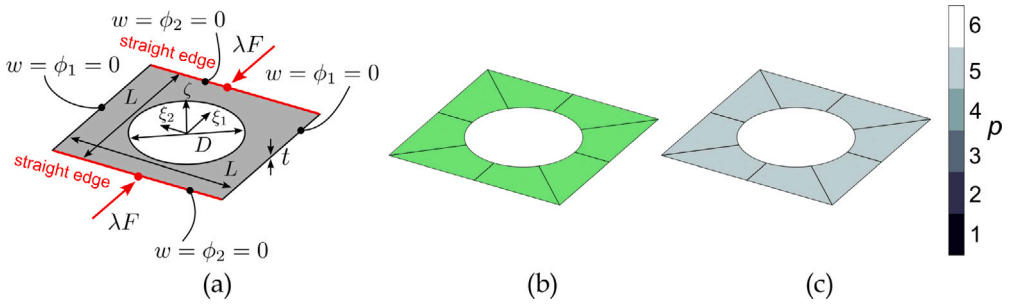

Fig. 8. Cutout plate problem. Geometric quantities are referred to the plate middle surface, while boundary conditions are defined in terms of middle displacement (u, v, w) and rotation (ϕ_1, ϕ_2) components in a cartesian reference system (ξ_1, ξ_2, ζ). The finite element model is defined in terms of mesh resolution h, and element polynomial order p.

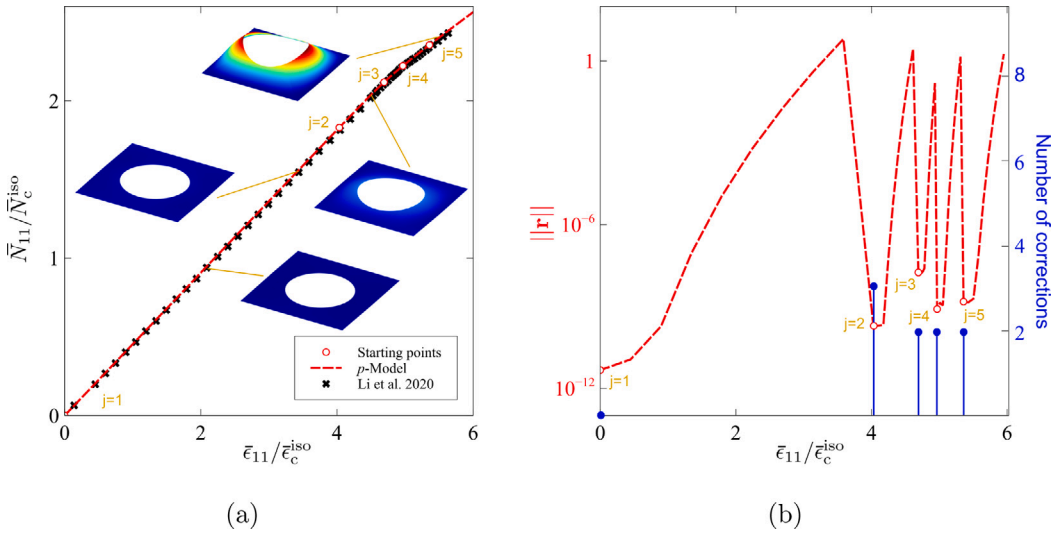

Fig. 9. Solution of the cutout plate problem. Solutions are presented in terms of load-shortening and error curves. The error curve is overlapped with a bar diagram showing the number of corrections for each prediction steps. Deflection shapes are plotted with a magnification factor of 30, while contour colors are generated in terms of $\sqrt{u^2 + v^2 + w^2}$ and normalized with a factor of 2 mm.

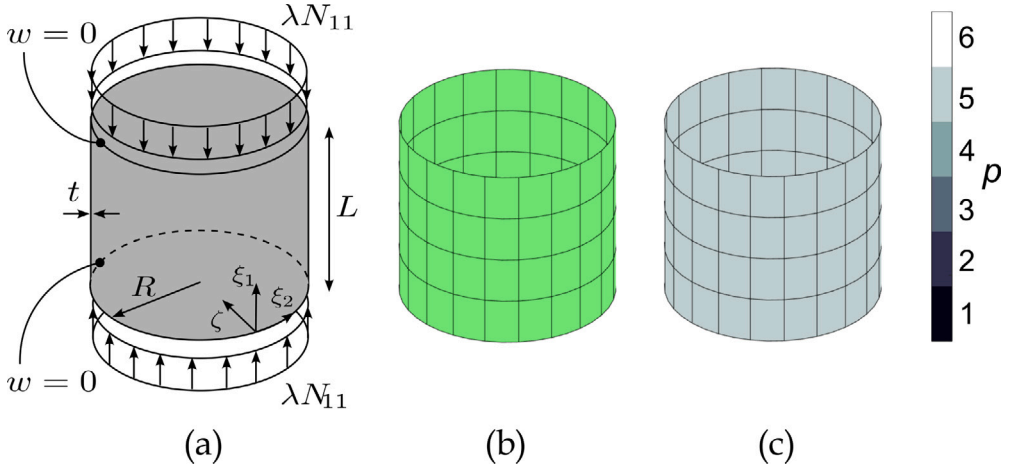

Fig. 10. Water's composite cylinder problem. Geometric quantities are referred to the cylinder's middle surface, while boundary conditions are defined in terms of middle displacement (u, v, w) and rotation (ϕ_1, ϕ_2) components in a cylindrical reference system (ξ_1, ξ_2, ζ). The finite element model is defined in terms of mesh resolution h, and element polynomial order p.

ply properties are: $E_{11} = 127,629$ MPa, $E_{22} = 11,307.4$ MPa, $G_{12} = G_{13} = G_{23} = 6,002.57$ GPa, $\nu_{12} = \nu_{23} = \nu_{13} = 0.300235$.

The shell is axially loaded with a uniformly distributed compression load applied along the top and bottom rim. Both the ends are subjected to simply-supported boundary conditions of type SS-3. The imperfections are introduced analytically considering a rectangular mode

$$w_0(x, y) = A_0 \sin\left(\frac{\pi m x}{L}\right) \cos\left(\frac{\pi n y}{R}\right), \tag{26}$$

with wave numbers $m = 1$ and $n = 7$, and imperfection amplitude $A_0 = 0.75t$. This imperfection shape drives the shell to a global deformation mode in the post-buckling range.

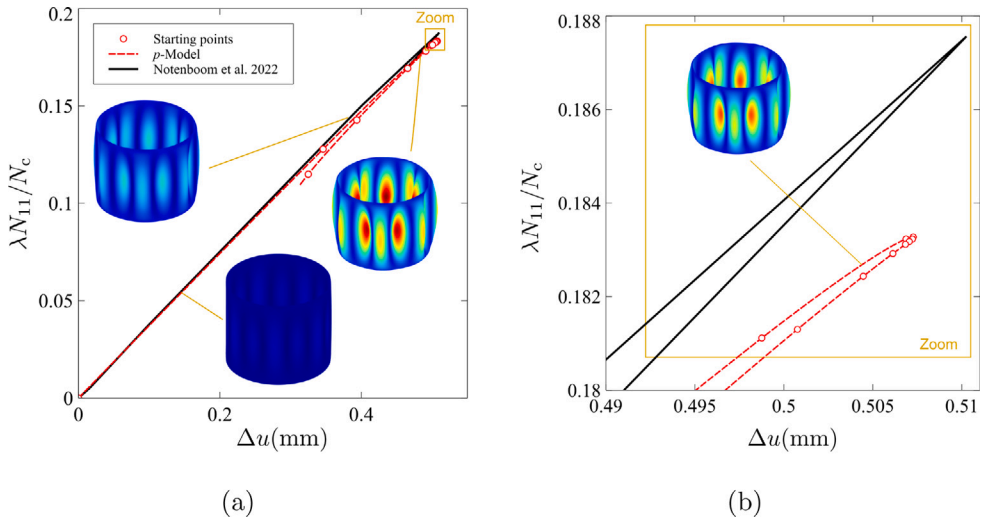

(a) (b)

Fig. 11. Solution of the Water's composite cylinder problem. The solution is presented in terms of a load-shortening curve. A zoom of the limit point is provided for better visualization. Deflection shapes are plotted with a magnification factor of 30, while contour colors are generated in terms of $\sqrt{u^2+v^2+w^2}$ and normalized with a factor of 2 mm.

The numerical model is presented in Fig. 10b-10c. It consists of a mesh with 20 elements along the circumferential direction and 4 along the axial one. Such a coarse mesh is justified by the adoption of a relatively high polynomial order for the elements, which is $p = 5$.

The load–displacement curves obtained with the present approach and the one taken from Ref. [74] are reported in Fig. 11. The load is expressed in terms of Loadscale Factor (LF), defined as the applied edge resultant N_{11} divided by the linearized buckling load, i.e. $N_c = 391.9888$ N/mm [72]. The end-shortening Δu is measured as the average shortening undergone by the cylinder.

The present results closely match with the ones obtained by Notenboom and Jansen [74], where a multi-modal perturbation method is employed as solution strategy. The limit LF predicted in Ref. [74] is 0.1875, while the one obtained with the present method is 0.1856. The percent difference between the two approaches is small, 2% approximately.

A further detail of the solution is provided in Fig. 11b, which illustrates a zoom around the limit load. The plot highlights the sharpness of the turning point, which can cause a premature analysis failure in arc-length methods, unless a careful tuning of the step size is performed. The selection of an appropriate step length entails a balancing between efficiency and convergence demands of the solver, which can be a very tedious and time-consuming process. Within the present approach this problem does not arise. Indeed, the ANM can adjust automatically the step size, which is very large in the linear pre-buckling path, while it gets smaller in correspondence of the limit point. Using the parameter shown in Table 3, the maximum and minimum steps size are $\xi_{\text{ROV}}^{\max} = 4.85$ and $\xi_{\text{ROV}}^{\min} = 0.08$, respectively. This step-length adjustment is performed without the user intervention. The only parameter to be tuned is the estimator's constant ϵ, whose value is chosen based on whether a short-steps/high-quality or a large-steps/low-quality solution is required.

Benchmark 1: Highly anisotropic plate

The analysis of highly anisotropic composite plates offers numerical challenges due to localization effects induced by drastic elastic couplings. The difficulties in evaluating buckling loads and linear frequencies have been investigated in past works in the literature [62,75,76]. Here, new reference results are derived with focus on the post-buckling response of these laminates. No previous attempts can be found in the literature, so reporting accurate results for this class of problems is believed of interest for future comparisons by other researchers.

The benchmark is taken from [76] and is presented in Fig. 12. It consists of a very thin square plate with side $L = 100$ mm and $L/t = 100,000$. This extremely high ratio L/t was considered in Ref. [76] to minimize shear deformation effects and have a fair comparison between a Ritz code based on Kirchhoff theory and Abaqus simulations. The plate is made of a single ply oriented at 45 degree, while the following material data are used: $E_{11} = 369,000$ MPa, $E_{22} = 5,030$ MPa, $G_{12} = G_{13} = G_{23} = 5,240$ MPa, $\nu_{12} = \nu_{23} = \nu_{13} = 0.31$. Simply-supported boundary conditions are considered, as they are associated with the mostly intricate linearized buckling response [76]. Hence, they are believed of particular interest even for the post-buckling case. The load is introduced by imposing uniform edge-shortening conditions. The unloaded edges are free to expand. A sketch of the structure and the relevant boundary conditions is available in Fig. 12a.

This benchmark is analyzed by means of three distinct numerical models. Following the nomenclature of Table 1, they are denoted as: *h*-Model, *p*-Model and *ps*-Model. In particular, the first one is generated and solved using Abaqus in the context of an *h*-refinement strategy and an IIP. The *p*-Model and the *ps*-Model are developed within the present FE framework using *p*- and *ps*-refinement strategies, respectively, and are solved with the ANM.

The meshes of the *h*- and *p*-Models are assembled from square elements of constant size. Regarding the *ps*-Model, its mesh is characterized by three levels of *s*-refinements and is illustrated in Fig. 12.

For this case, the mesh design is based on the studies of Ref. [62], which showed the occurrence of complex anisotropy-induced local effects around two opposite corners. In these regions, concentrations of twisting moment and transverse shear are observed. Therefore, local refinements are introduced in these areas. The color code of Fig. 12c clarifies how successive mesh layers are generated with polynomials of decreasing order.

The results for the different numerical models are reported in Fig. 13 in terms of load–deflection, see Figs. 13a, 13c and 13e, and load–stress curves, see Figs. 13b, 13d and 13f. Load and deflections are expressed in adimensional form using the critical load λ_c and thickness t.

The curves in Figs. 13a-13b show a convergence study on the Abaqus-generated *h*-Model. Looking at the number of DOFs, one can have an idea of the convergence challenges of this problem. Adopting an *h*-refinement strategy, 61,206 DOFs are still insufficient to capture correctly the bifurcation point. To reach a stable and consistent value for displacements and stresses in the solution range of interest, a total

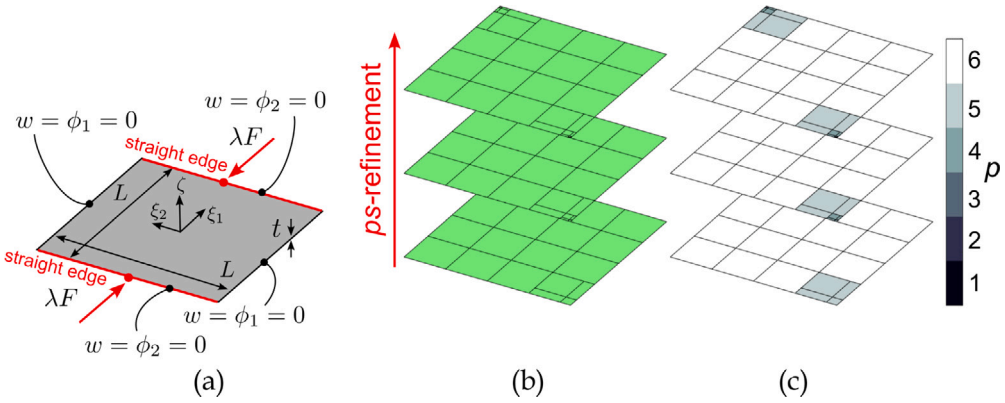

Fig. 12. Highly anisotropic plate problem. Geometric quantities are referred to the plate middle surface, while boundary conditions are defined in terms of middle displacement (u, v, w) and rotation (ϕ_1, ϕ_2) components in a cartesian reference system (ξ_1, ξ_2, ζ). The finite element model is defined in terms of mesh resolution h, and element polynomial order p for three different levels of ps-refinement.

Table 5
Comparison of performance between different FE formulations — highly anisotropic plate.

Model	Refinement level	$\eta_{\%}$	$E_{\%}$[a] for $w(0,0)$	$E_{\%}$[a] for $\sigma_{11}(0,0,t/2)$
h-Model	1	1.09	14.88	20.57
	2	4.16	5.25	6.50
	3	25.25	1.37	1.26
	4	100.00	0.00	0.00
p-Model	1	3.30	87.20	94.39
	2	7.43	19.45	11.89
	3	13.21	12.62	9.93
ps-Model	1	1.44	10.95	8.33
	2	1.58	5.78	4.11
	3	1.66	2.87	1.78

[a] Error are measured considering quantities at load step $\lambda/\lambda_c = 1.2$.

of 242,406 DOFs are necessary. This is a relatively large model for plate problem.

The results of the p-Model considering a 20×20 mesh are shown in Figs. 13c-13d. In this case, the p-refinement strategy exhibits an even worse convergence rate. Quartic shape functions still do not lead to a satisfactory accuracy, as evident from the zooms around the bifurcation point. The poor performance of the p-refinement strategy is explained by the inadequacy of high-order polynomials to capture the low-spatial-frequency effects. In general, these are better represented via low-order/piece-wise approximations, rather than high-order/continuous ones.

The simulations with the ps-Model are reported in Figs. 13e-13f. This model shows the fastest convergence rate among the ones considered earlier. The superior efficiency is achieved thanks to a more effective refinement strategy: large/high-order elements are employed in smooth solution regions, while small/low-order elements are used in proximity of steep gradients.

To gather further insight into the performance of the different refinement strategies, a direct comparison between the three models is presented in Table 5.

Two parameters are introduced for this purpose, the percent error $E_{\%}$ and the DOFs ratio

$$\eta_{\%} = \frac{N_{\text{DOF}}^{\text{FE}}}{242,406} \times 100 \tag{27}$$

relative to the converged h-Model.

The results of the p-Model quantify the inadequacy of the p-refinement strategy for the problem at hand. The percentage errors at refinement level 3 (32,019 DOFs) are one order of magnitude larger than the ones of h-Model at refinement level 2 (10,086 DOFs), despite the latter is associated with 1/3 the number of DOFs of the former. When considering the ps-approach, satisfactory accuracy is achieved at refinement level 3 (4,023 DOFs), which corresponds to $1 - 2\%$ the number of DOFs of the converged h-Model. So, the reduction of the problem size is drastic.

Benchmark 2: "Dog-bone" shell

In this test case, the postbuckling analysis of a VS cylindrical panel with a "dog-bone" shape is investigated. The problem is illustrated in Fig. 14, where the following geometric data are considered: $a = 200$ mm, $b = 100$ mm, $a_1 = b_1 = 60$ mm, $R = 500$ mm, $t = 1$ mm. The VS stacking sequence is described by $[\pm\langle 30, 0\rangle]_{4s}$, with fibers varying along the circumferential direction.

The material considered is P100/AS3501 [75], a pre-preg with high levels of anisotropy with mechanical properties: $E_{11} = 369,000$ MPa, $E_{22} = 5,030$ MPa, $G_{12} = G_{13} = G_{23} = 5,240$ MPa, $\nu_{12} = \nu_{23} = \nu_{13} = 0.31$. Simply-supported conditions are imposed at $\xi_1 = \pm a/2$ and $\xi_2 = \pm b/2$, while the re-entrant edges are free. The curved sides are loaded with a uniform edge-shortening, while the unloaded ones are prevented to expand in the transverse direction. The post-buckling analysis is carried out considering an imperfection whose amplitude is 50% the wall thickness t and shape of the first buckling mode.

The structure is analyzed using two different strategies, aiming at illustrating the advantages offered by the present FE framework. The first approach relies on the standard strategy considered in commercial FE codes: an h-Model is used for the numerical description of the structure along with a Riks-based solution procedure. In this case, the simulations are conducted using Abaqus. The second approach relies on an advanced ps-Model in conjunction with the ANM solution procedure.

The features of the numerical models and solution algorithms are summarized in Tables 2 and 3, respectively. The mesh of the ps-Models is reported in Figs. 14b-14c. The presence of internal corners suggests the introduction of local refinements to appropriately capture sharp gradients occurring in these areas. As seen, three levels of refinement

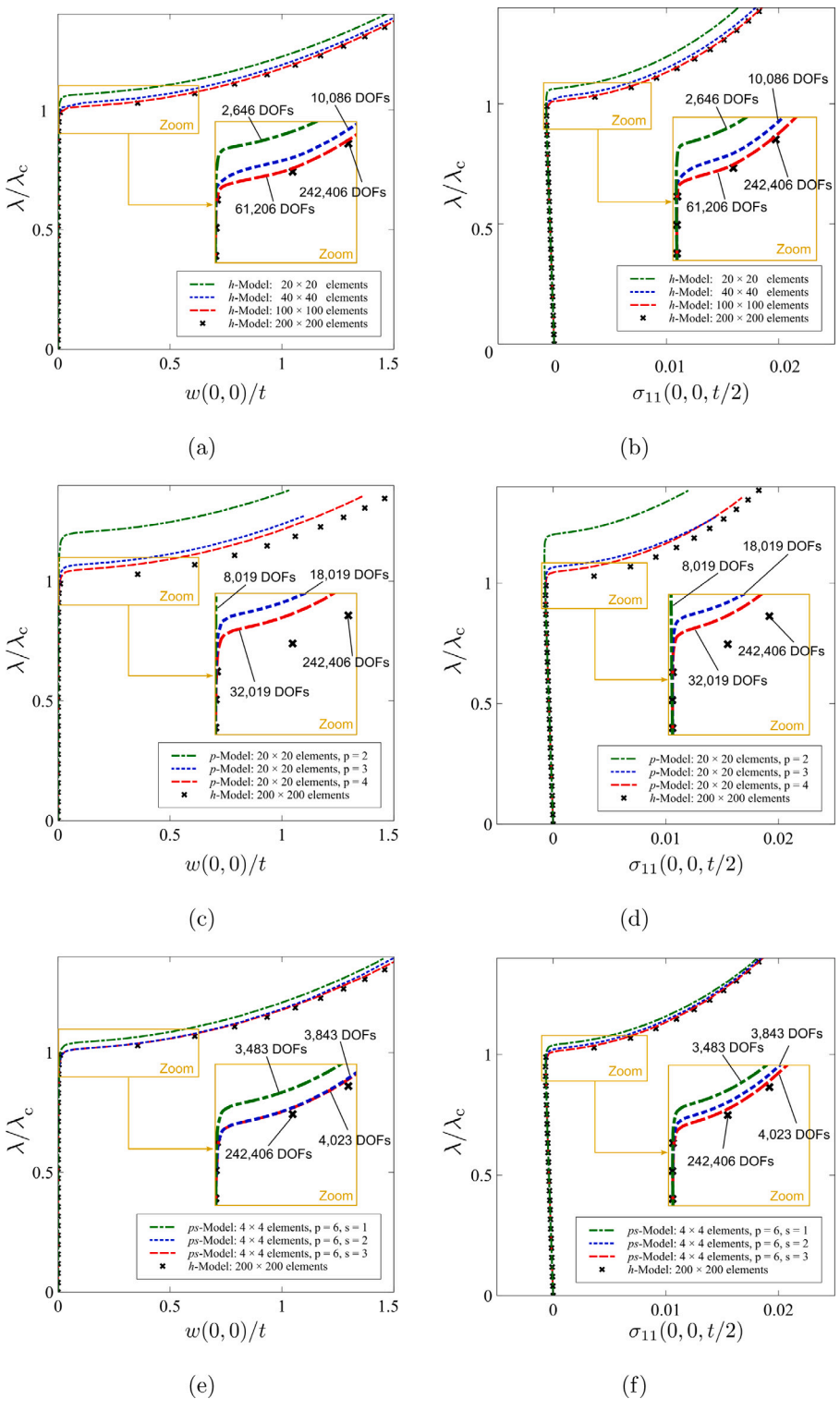

Fig. 13. Solution of the highly anisotropic plate problem. The first column reports load–deflection curves. The second column reports load–stress curves. Rows refer to the curves obtained with different finite element models: *h*-Model (first row), *p*-Model (second row) and *ps*-Model (third row).

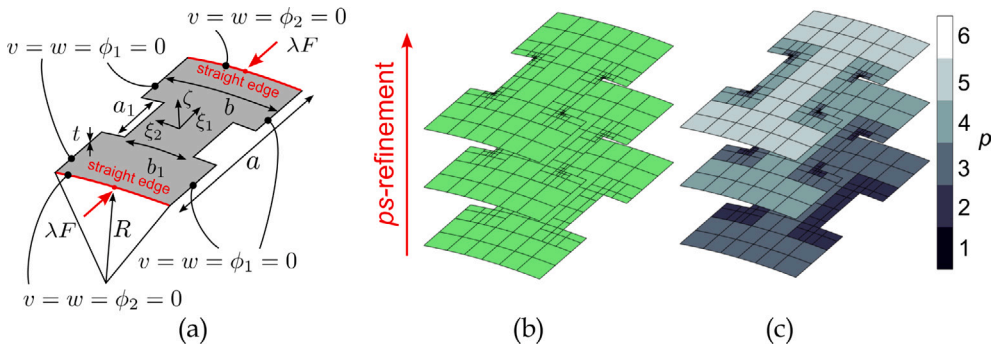

Fig. 14. "Dog-bone" shell problem. Geometric quantities are referred to the shell middle surface, while boundary conditions are defined in terms of middle displacement (u, v, w) and rotation (ϕ_1, ϕ_2) components in a curvilinear reference system (ξ_1, ξ_2, ζ). The finite element model is defined in terms of mesh resolution h, and element polynomial order p for three different levels of *ps*-refinement.

Table 6
Comparison of performance between different solution algorithms – "dog-bone" shell.

Algorithm	Steps	Corrections per step	Factorizations	Residual eval.	$\mathbf{q}_k$ eval.[a]
IIP	100	3	100×3	100×3	/
ANM	11	2	$11 + (11 \times 2)$	11×2	11×15

[a] CPU similar to a residual evaluation.

are considered, with progressive reduction of the element size and polynomial order.

The results of the *h*-Model are presented in Figs. 15a-15b in terms of load–deflection and load–stress curves.

A large number of elements is necessary to guarantee converged displacements and stresses. This is due to the presence of free and re-entrant edges, which are responsible for local stress concentrations. Moreover, the non-uniform stiffness distribution and high level of material anisotropy generate a relatively intricate internal load path. As a consequence, the *h*-Model requires a total number of 18,832 elements, corresponding to 115,110 DOFs.

The results of the *ps*-Model are reported in Figs. 15c-15d with the converged *h*-Model. In this case, 44 elements of order $p = 5$ and $s = 3$ layers of overlaying meshes suffice to achieve satisfactory results. The corresponding number of DOFs is 9,318 DOFs, which represents less than 92% the DOFs of the converged *h*-Model. This computational savings can be further magnified by adopting the ANM for solving the *ps*-Model.

A performance comparison between the ANM and the Riks method is presented in Table 6.

With a minimum and maximum arc-length increment of 10^{-5} and 10^{-1}, respectively, and a tolerance of 5×10^{-3}, the Riks method requires a total of 100 increment steps from the undeformed configuration to the post-buckling state corresponding to $F = 1944$ N. The average number of iterations per increment is 3. Accordingly, a number of ≈300 matrix factorizations and residual evaluations are necessary to complete the analysis. On the other hand, the ANM requires only 11 prediction steps, with an average of 2 iterations to perform the Newton–Raphson correction. It is worth noting that less correction steps are required in this case, even if the tolerance is 3–4 order of magnitudes stricter than the one used in Abaqus — see Table 3.

The reduced number of prediction steps possible with the ANM enables a considerable drop of required matrix factorizations. Moreover, the matrices to be inverted have smaller size due to the advanced refinement procedures available in the *ps*-FEM. These features lead to significant improvements in terms of computational efficiency.

Benchmark 3: Conical shell

This benchmark problem considers a conical composite shell loaded in compression with a perturbation force acting in the transverse direction. The challenging features of this test case involve the presence of an unstable post-buckling response and the stress concentrations induced by the perturbation load.

The cone under investigation is taken from Ref. [77] and is illustrated in Fig. 16 with its finite element discretization. The shell is defined by the following geometric properties: $H = 200$ mm, $R = 400$ mm, $\alpha = 45$ deg, and $t = 1.1250$ mm. The material elastic properties of the material are: $E_{11} = 142,500$ MPa, $E_{22} = 8,700$ MPa, $G_{12} = G_{13} = G_{23} = 5,100$ MPa, $\nu_{12} = \nu_{23} = \nu_{13} = 0.28$. The lamination sequence is defined by the 9-plies layup $[\pm 30/\pm 60/0]_{\text{ms}}$, where the subscript *ms* denotes mid-plane symmetry, meaning that the ply at 0 is not repeated.

The boundary conditions are simply-supported of SS1 type, as shown in Fig. 16a. The compressive load is applied by imposing an axial displacement to the nodes of the upper edge. This condition is denoted in the figure as *no-warping edge*. The perturbation load F_{SPL} is introduced at the shell mid-height, and acts along the shell normal direction. The loading sequence consists in the initial application of the perturbation load of 50 N, followed by the axial compression. During this second phase, the perturbation load is maintained constant at 50 N.

For this problem, a *ps*-Model is employed, see Fig. 16b-16c. The mesh has a resolution of 4×20 elements with order $p = 5$. The combination of a relatively coarse mesh with high-order elements proved to be a good tradeoff between computational cost and accuracy in predicting the buckling load. A number of $s = 3$ levels of superposition meshes are introduced around the point of application of the force to capture the local features of the solution.

The solution of the numerical model is performed using the ANM with the parameters of Table 3. The load–displacement curves are reported in Fig. 17, where the comparison is presented against Abaqus simulations.

The *h*-Model is generated with 270×90 elements and used in conjunction with the Riks method. The nonlinear solution is characterized by an initial Local Snap-Through (LST), followed by a Global Buckling (GB) response. Both these effects are captured by the *ps*-Model. In particular, the LST and GB points are predicted at the load levels of $F_{\text{LST}} = 63.970$ kN and $F_{\text{GB}} = 85.335$ kN, respectively. The corresponding points extracted from Abaqus simulations are $F_{\text{LST}} = 65.253$ kN and $F_{\text{GB}} = 85.260$ kN.

The *ps*-Model is characterized by less than 1/10 the DOFs required by the *h*-Model. As shown, this saving does not imply any loss of

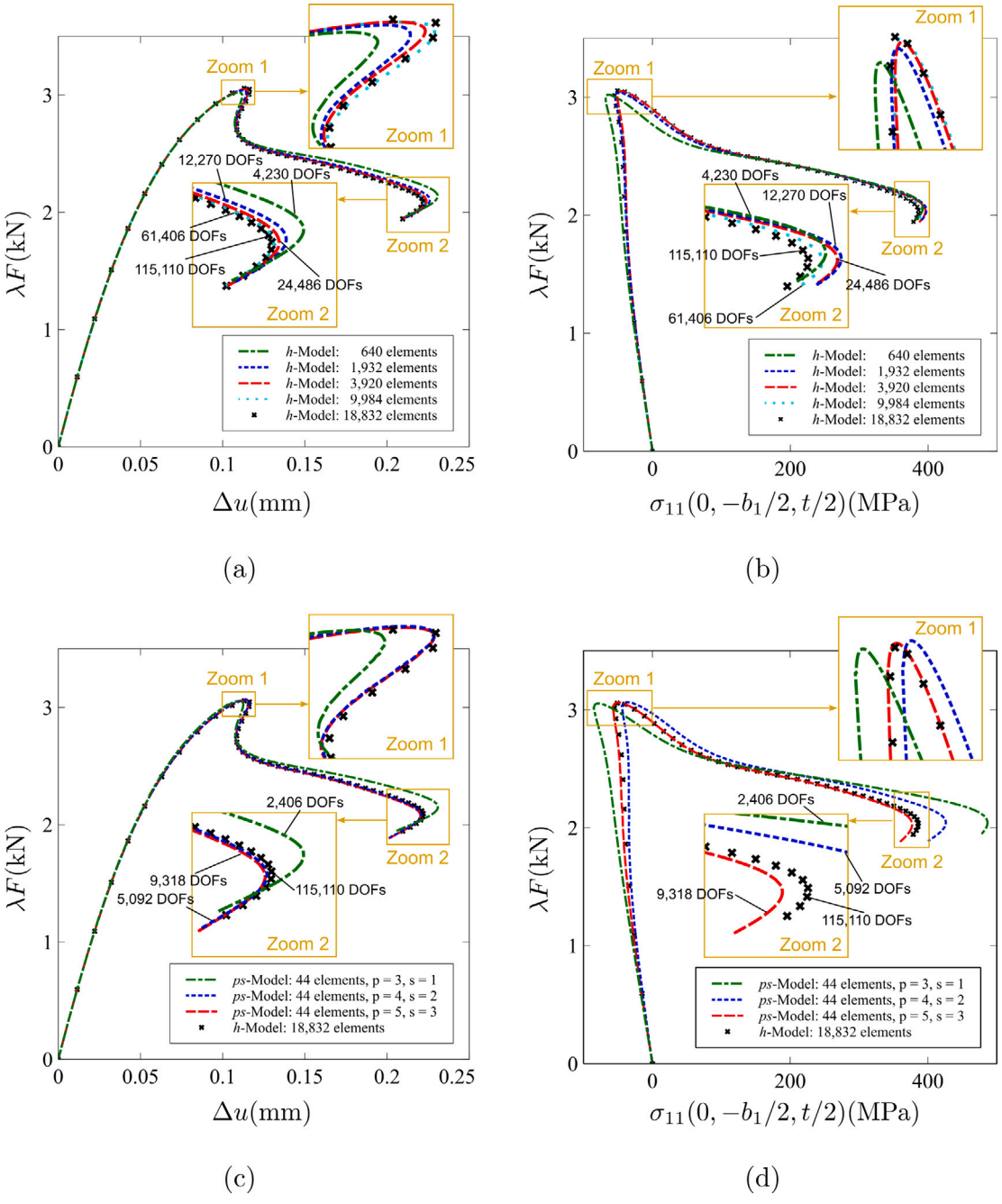

Fig. 15. Solution of the "dog-bone" shell problem. The first column reports load-shortening curves. The second column reports load–stress curves. Rows refer to the curves obtained with different finite element models: *h*-Model (first row) and *ps*-Model (second row).

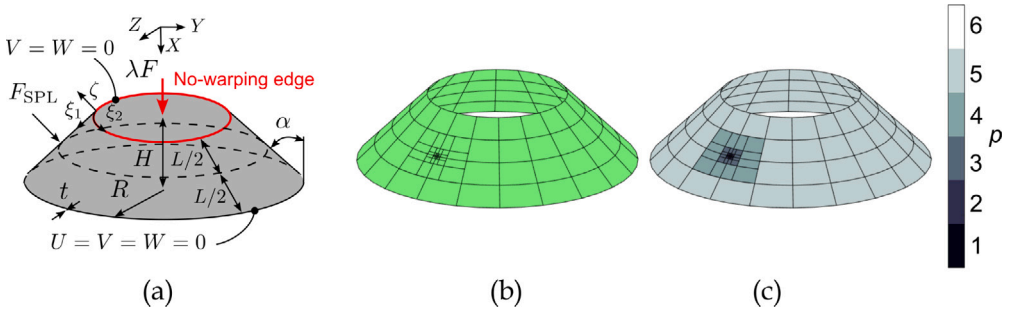

Fig. 16. Conical shell problem. Geometric quantities are referred to the cone's middle surface, while boundary conditions are defined in terms of middle displacement (U, V, W) in a cartesian reference system (X, Y, Z). The finite element model is defined in terms of mesh resolution h, and element polynomial order p.

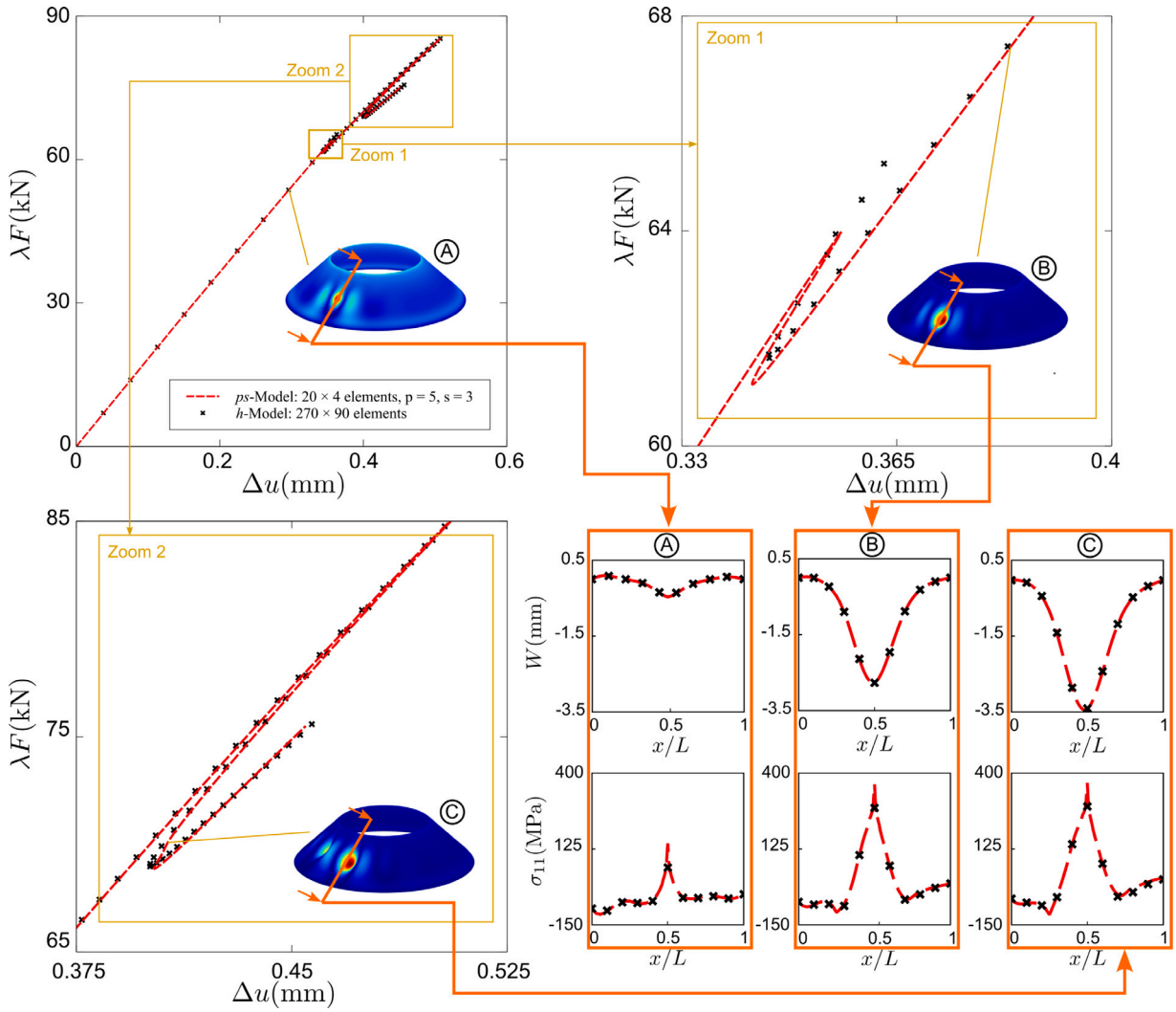

Fig. 17. Solution of the conical shell problem. The solution is presented in terms of load-shortening curves. Two zooms are provided for better visualization of the local snap-through and global buckling. Deflection shapes are plotted with a magnification factor of 10, while contour colors are generated in terms of $\sqrt{u^2+v^2+w^2}$. For each deflection mode displacement W and stress σ_{11} profiles are provided at $\xi_2 = 0$.

accuracy. On the contrary, the *ps*-Model provides a slightly smaller prediction for F_{LST}, likely achievable through further refinement of the Abaqus model.

In Fig. 17 are also shown displacement and stress profiles at $\xi_2 = 0$ for different equilibrium points, which are here denoted as A, B and C. Point A is taken in the pre-buckling region ($F = 53.69$ kN), point B is located in the region between the LST and the GB ($F = 67.43$ kN), while C is chosen in the region after GB has occurred ($F = 69.92$ kN). From the plots of Fig. 17, it is possible to see that the *ps*- and *h*-Models predict a similar global trend for the deflection and direct stress. Not surprisingly, the stress singularity induced by the concentrated force is better represented by the present approach, owing to the presence of a local refinement.

6. Conclusions

This work introduces a computational tool for nonlinear shell analysis based on two pillars: the *ps*-FEM, used for the spatial discretization, and the ANM, used for the solution of the discrete problem. The synergy of these elements results in a novel analysis framework capable of performing much quicker and more accurate nonlinear analyses compared to traditional approaches.

One of the key aspects of this study regards the improved efficiency of the *ps*-FEM over standard FE- and Ritz-based methods. In particular, the results illustrate that saving in DOFs as high as 90% are achievable by a proper refinement procedure. The *ps*-FEM employs a combination of *p*- and *s*-refinements, such that large/high-order elements are placed in smooth solution regions, while small/low-order elements are overlaid in areas of localized effects. These features are not attainable with a Ritz approach, while they involve complex mesh generations in FE methods.

A second aspect of this work concerns the use of the ANM as solver to further leverage the advantages of the *ps*-FEM. By employing a piece-wise analytic representation of the nonlinear solution, the ANM tracks the equilibrium path with different prediction, estimation, and correction steps. For the problems investigated here, the resulting number of increments/iterations is drastically smaller with respect to an incremental-iterative procedure. In particular, a reduction of a factor of 10 in number of matrix factorizations is observed compared to the Riks method, leading to a further drop in cpu.

Based on these aspects, it is concluded that the combination of *ps*-FEM and ANM is a viable strategy to optimize the time for the analysis from several perspectives: the numerical solution has faster convergence, the modeling phase is simplified, the solution procedure requires fewer computer operations. All these features make the proposed tool

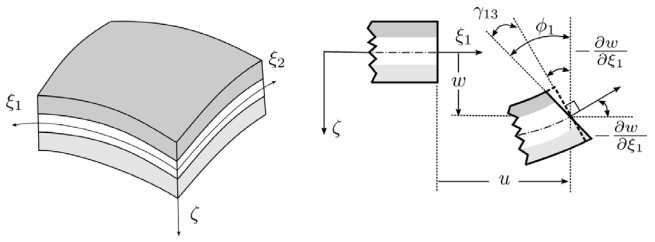

Fig. 18. Reference system and kinematics of the shell. The mathematical model is defined from a First-order Shear Deformation Theory (FSDT). The formulation of the theory is done on a curvilinear reference system so that generic shell configurations can be considered.

an interesting mean for the design and analysis of advanced composite shell structures, especially when the process may benefit from early introduction of nonlinear requirements.

CRediT authorship contribution statement

C.A. Yan: Writing – original draft, Validation, Software, Methodology, Investigation, Formal analysis, Conceptualization. **R. Vescovini:** Writing – review & editing, Supervision, Investigation.

Declaration of competing interest

The authors declare that they have no known competing financial interests or personal relationships that could have appeared to influence the work reported in this paper.

Data availability

No data was used for the research described in the article.

Appendix

Definition of the shell mathematical model

The mathematical model considered in this work is based on a first-order shell theory. Accordingly, the displacement field $\{u_1, u_2, u_3\}^{\mathrm{T}}$ is expressed as function of the displacements $\{u, v, w\}^{\mathrm{T}}$ and rotations $\{\phi_1, \phi_2\}^{\mathrm{T}}$ components on the shell's middle surface Ω, see Fig. 18. In this work, the middle surface is parametrized by two arc-length coordinates ξ_1 and ξ_2, so that an orthogonal curvilinear coordinate system (ξ_1, ξ_2, ζ) can be defined to describe the shell kinematics, with ζ being the coordinate normal to Ω.

The components of the Green–Lagrange strain tensor $E_{\alpha\beta}$, are arranged in two vectors $\boldsymbol{\epsilon} = \{E_{11}\ E_{22}\ 2E_{12}\}^{\mathrm{T}}$ and $\boldsymbol{\gamma} = \{2E_{13}\ 2E_{23}\}^{\mathrm{T}}$, so that

$$\boldsymbol{\epsilon} = \boldsymbol{\epsilon}^0 + \zeta\mathbf{k}, \quad \text{and} \quad \boldsymbol{\gamma} = \boldsymbol{\gamma}^0. \tag{28}$$

The vector of generalized membrane strains $\boldsymbol{\epsilon}^0$, curvatures $\mathbf{k}$, and shear strains $\boldsymbol{\gamma}_0$ in Eq. (28) are available in Ref. [62]. The corresponding generalized forces are obtained from the constitutive law

$$\begin{Bmatrix}\mathbf{N}\\ \mathbf{M}\end{Bmatrix} = \begin{bmatrix}\mathbf{A}(\xi_1,\xi_2) & \mathbf{B}(\xi_1,\xi_2)\\ \mathbf{B}(\xi_1,\xi_2) & \mathbf{D}(\xi_1,\xi_2)\end{bmatrix}\begin{Bmatrix}\boldsymbol{\epsilon}^0\\ \mathbf{k}\end{Bmatrix} \quad \text{and} \quad \mathbf{Q} = \overline{\mathbf{A}}(\xi_1,\xi_2)\boldsymbol{\gamma}^0, \tag{29}$$

where $\mathbf{N} = \{N_{11}\ N_{22}\ N_{12}\}^{\mathrm{T}}$, $\mathbf{M} = \{M_{11}\ M_{22}\ M_{12}\}^{\mathrm{T}}$, $\mathbf{Q} = \{Q_1\ Q_2\}^{\mathrm{T}}$ represent the force and moment resultants, whereas $\mathbf{A}$, $\mathbf{D}$, $\mathbf{B}$, $\overline{\mathbf{A}}$ are the membrane, stiffness, coupling and transverse shear stiffness matrices. These matrices are assumed to be function of the in-plane coordinates, so that modern Variable-Stiffness laminates [78–80] can be accounted for.

The expression of the mixed functional Π^* and its variations $\delta\Pi^*$ are given by

$$\begin{aligned}\Pi^*(\mathbf{u},\mathbf{S}) = \int_\Omega \Big[\big(\boldsymbol{\epsilon}^{0\mathrm{T}}\mathbf{N} + \mathbf{k}^{\mathrm{T}}\mathbf{M} + \boldsymbol{\gamma}^{0\mathrm{T}}\mathbf{Q}\big) - \frac{1}{2}\big(\mathbf{N}^{\mathrm{T}}\mathbf{A}^*\mathbf{N} + \mathbf{M}^{\mathrm{T}}\mathbf{D}^*\mathbf{M} +\\ + 2\mathbf{N}^{\mathrm{T}}\mathbf{B}^*\mathbf{M}\mathbf{Q}^{\mathrm{T}}\overline{\mathbf{A}}^*\mathbf{Q}\big)\Big]\,\mathrm{d}\Omega + V(\mathbf{u}),\end{aligned} \tag{30}$$

$$\begin{aligned}\delta\Pi^*(\mathbf{u},\mathbf{S}) = \int_\Omega \big[\delta\boldsymbol{\epsilon}^{0\mathrm{T}}\mathbf{N} - \delta\mathbf{N}^{\mathrm{T}}\left(\boldsymbol{\epsilon}^0 - \mathbf{A}^*\mathbf{N} - \mathbf{B}^*\mathbf{M}\right) +\\ + \delta\mathbf{k}^{\mathrm{T}}\mathbf{M} - \delta\mathbf{M}^{\mathrm{T}}\left(\mathbf{k} - \mathbf{B}^*\mathbf{N} - \mathbf{D}^*\mathbf{M}\right) +\\ + \delta\boldsymbol{\gamma}^{0\mathrm{T}}\mathbf{Q} - \delta\mathbf{Q}^{\mathrm{T}}\left(\boldsymbol{\gamma}^0 - \overline{\mathbf{A}}^*\mathbf{Q}\right)\big]\,\mathrm{d}\Omega + \delta V(\mathbf{u}) = 0,\end{aligned} \tag{31}$$

respectively, where $V(\mathbf{u})$ is the potential of the applied loads, $\mathbf{A}^*, \mathbf{B}^*, \mathbf{D}^*$, $\overline{\mathbf{A}}^*$ are matrices obtained by inverting the constitutive law in Eq. (29), while the mixed unknowns are $\mathbf{u} = \{u, v, w, \phi_1, \phi_2\}^{\mathrm{T}}$ and $\mathbf{S} = \{\mathbf{N}, \mathbf{M}, \mathbf{Q}\}^{\mathrm{T}}$.

Definition of the mixed problem

Using the following notation for the generalized strains

$$\begin{aligned}&\boldsymbol{\epsilon}^0 = \boldsymbol{\epsilon}^0_1(\mathbf{u}) + \frac{1}{2}\boldsymbol{\epsilon}^0_2(\mathbf{u}), \qquad \mathbf{k} = \mathbf{k}(\mathbf{u}), \qquad \boldsymbol{\gamma}^0 = \boldsymbol{\gamma}^0(\mathbf{u}),\\ &\delta\boldsymbol{\epsilon}^0 = \boldsymbol{\epsilon}^0_1(\delta\mathbf{u}) + \boldsymbol{\epsilon}^0_{11}(\delta\mathbf{u},\mathbf{u}), \qquad \delta\mathbf{k} = \mathbf{k}(\delta\mathbf{u}), \qquad \delta\boldsymbol{\gamma}^0 = \boldsymbol{\gamma}^0(\delta\mathbf{u}),\end{aligned} \tag{32}$$

the linear $L(\cdot)$, quadratic $Q(\cdot,\cdot)$, constant F operators are

$$\begin{aligned}\delta\mathbf{U}\cdot L(\mathbf{U}) &= \begin{Bmatrix}\int_\Omega[\boldsymbol{\epsilon}^0_1(\delta\mathbf{u})^{\mathrm{T}}\mathbf{N} + \mathbf{k}(\delta\mathbf{u})^{\mathrm{T}}\mathbf{M} + \boldsymbol{\gamma}^0(\delta\mathbf{u})^{\mathrm{T}}\mathbf{Q}]\mathrm{d}\Omega\\ \int_\Omega[\delta\mathbf{N}^{\mathrm{T}}(\boldsymbol{\epsilon}^0_1(\mathbf{u}) - \mathbf{A}^*\mathbf{N} - \mathbf{B}^*\mathbf{M}) + \delta\mathbf{M}^{\mathrm{T}}(\mathbf{k}(\mathbf{u}) - \mathbf{B}^*\mathbf{N} - \mathbf{D}^*\mathbf{M}) +\\ +\delta\mathbf{Q}^{\mathrm{T}}(\boldsymbol{\gamma}^0(\mathbf{u}) - \overline{\mathbf{A}}^*\mathbf{Q})]\mathrm{d}\Omega\end{Bmatrix},\\ \delta\mathbf{U}\cdot Q(\mathbf{U},\mathbf{U}) &= \begin{Bmatrix}\int_\Omega \boldsymbol{\epsilon}^0_{11}(\delta\mathbf{u},\mathbf{u})^{\mathrm{T}}\mathbf{N}\mathrm{d}\Omega\\ \int_\Omega \delta\mathbf{N}^{\mathrm{T}}\frac{1}{2}\boldsymbol{\epsilon}^0_2(\mathbf{u})\mathrm{d}\Omega\end{Bmatrix}, \quad \text{and}\\ \delta\mathbf{U}\cdot F &= \begin{Bmatrix}-V(\delta\mathbf{u})\\ 0\end{Bmatrix}.\end{aligned} \tag{33}$$

Change of formulation

The generic mixed problem of order $k \geq 1$ is

$$T(\mathbf{U}_k) = \lambda_k F - \sum_{r=1}^{k-1} Q(\mathbf{U}_r, \mathbf{U}_{k-r}). \tag{34}$$

The explicit form of Eq. (34) reads as the equation given in Box I, where the following formalism for the quadratic operator is used

$$\delta\mathbf{U}\cdot Q(\mathbf{U}_a,\mathbf{U}_b) = \begin{Bmatrix}\int_\Omega[\boldsymbol{\epsilon}^0_{11}(\delta\mathbf{u},\mathbf{u}_a)^{\mathrm{T}}\mathbf{N}_b + \boldsymbol{\epsilon}^0_{11}(\delta\mathbf{u},\mathbf{u}_b)^{\mathrm{T}}\mathbf{N}_a]\mathrm{d}\Omega\\ \int_\Omega \delta\mathbf{N}^{\mathrm{T}}\boldsymbol{\epsilon}^0_{11}(\mathbf{u}_a,\mathbf{u}_b)\mathrm{d}\Omega\end{Bmatrix}. \tag{35}$$

The mixed linear problem in Eq. I is equivalent to a pseudo-equilibrium condition

$$\begin{aligned}&\int_\Omega[\boldsymbol{\epsilon}^0_{11}(\delta\mathbf{u},\mathbf{u}_k)^{\mathrm{T}}\mathbf{N}_0 + (\boldsymbol{\epsilon}^0_1(\delta\mathbf{u}) + \boldsymbol{\epsilon}^0_{11}(\delta\mathbf{u},\mathbf{u}_0))^{\mathrm{T}}\mathbf{N}_k + \mathbf{k}(\delta\mathbf{u})^{\mathrm{T}}\mathbf{M}_k +\\ &+\boldsymbol{\gamma}^0(\delta\mathbf{u})^{\mathrm{T}}\mathbf{Q}_k]\mathrm{d}\Omega = -\lambda_k V(\delta\mathbf{u}) - \sum_{r=1}^{k-1}\int_\Omega \boldsymbol{\epsilon}^0_{11}(\delta\mathbf{u},\mathbf{u}_{k-r})^{\mathrm{T}}\mathbf{N}_r\mathrm{d}\Omega,\end{aligned} \tag{36}$$

which is obtained from Eq. I by collecting terms multiplied by $\delta\mathbf{u} = \{\delta u, \delta v, \delta w, \delta\phi_1, \delta\phi_2\}^{\mathrm{T}}$, and a pseudo-constitutive law

$$\begin{aligned}\mathbf{N}_k &= \mathbf{A}[\boldsymbol{\epsilon}^0_1(\mathbf{u}_k) + \boldsymbol{\epsilon}^0_{11}(\mathbf{u}_0,\mathbf{u}_k) + \sum_{r=1}^{k-1}\frac{1}{2}\boldsymbol{\epsilon}^0_{11}(\mathbf{u}_r,\mathbf{u}_{k-r})] + \mathbf{B}\mathbf{k}(\mathbf{u}_k),\\ \mathbf{M}_k &= \mathbf{B}[\boldsymbol{\epsilon}^0_1(\mathbf{u}_k) + \boldsymbol{\epsilon}^0_{11}(\mathbf{u}_0,\mathbf{u}_k) + \sum_{r=1}^{k-1}\frac{1}{2}\boldsymbol{\epsilon}^0_{11}(\mathbf{u}_r,\mathbf{u}_{k-r})] + \mathbf{D}\mathbf{k}(\mathbf{u}_k),\\ \mathbf{Q}_k &= \overline{\mathbf{A}}\boldsymbol{\gamma}^0(\mathbf{u}_k),\end{aligned} \tag{37}$$

which is extracted from Eq. I by taking the terms multiplied by the virtual variation $\delta\mathbf{S} = \{\delta\mathbf{N}, \delta\mathbf{M}, \delta\mathbf{Q}\}^{\mathrm{T}}$. Finally, a substitution of Eq.

$$\left\{\begin{array}{c}\int_\Omega[\epsilon_1^0(\delta\mathbf{u})^{\mathrm{T}}\mathbf{N}_k+\mathbf{k}(\delta\mathbf{u})^{\mathrm{T}}\mathbf{M}_k+\boldsymbol{\gamma}^0(\delta\mathbf{u})^{\mathrm{T}}\mathbf{Q}_k]\mathrm{d}\Omega\\ \int_\Omega[\delta\mathbf{N}^{\mathrm{T}}(\epsilon_1^0(\mathbf{u}_k)-\mathbf{A}^*\mathbf{N}_k-\mathbf{B}^*\mathbf{M}_k)+\delta\mathbf{M}^{\mathrm{T}}(\mathbf{k}(\mathbf{u}_k)-\mathbf{B}^*\mathbf{N}_k-\mathbf{D}^*\mathbf{M}_k)+\delta\mathbf{Q}^{\mathrm{T}}(\boldsymbol{\gamma}^0(\mathbf{u}_k)-\overline{\mathbf{A}}^*\mathbf{Q}_k)]\mathrm{d}\Omega\end{array}\right\}+$$
$$+\left\{\begin{array}{c}\int_\Omega[\epsilon_{11}^0(\delta\mathbf{u},\mathbf{u}_k)^{\mathrm{T}}\mathbf{N}_0+\epsilon_{11}^0(\delta\mathbf{u},\mathbf{u}_0)^{\mathrm{T}}\mathbf{N}_k]\mathrm{d}\Omega\\ \int_\Omega\delta\mathbf{N}^{\mathrm{T}}\epsilon_{11}^0(\mathbf{u}_0,\mathbf{u}_k)\mathrm{d}\Omega\end{array}\right\}=-\lambda_k\left\{\begin{array}{c}V(\delta\mathbf{u})\\0\end{array}\right\}-\sum_{r=1}^{k-1}\left\{\begin{array}{c}\int_\Omega\epsilon_{11}^0(\delta\mathbf{u},\mathbf{u}_{k-r})^{\mathrm{T}}\mathbf{N}_r\mathrm{d}\Omega\\ \int_\Omega\delta\mathbf{N}^{\mathrm{T}}\frac{1}{2}\epsilon_{11}^0(\mathbf{u}_r,\mathbf{u}_{k-r})\mathrm{d}\Omega\end{array}\right\},$$

Box I.

(37) into Eq. (36) leads to the displacement version of Eq. I. The corresponding numerical solution can be obtained after applying a FE discretization.

References

[1] Babuška I, Szabó BA, Katz IN. The p-version of the finite element method. SIAM J Numer Anal 1981;18(3):515–45.
[2] Babuška I, Dorr MR. Error estimates for the combined h and p versions of the finite element method. Numer Math 1981;37(2):257–77.
[3] Rank E, Düster A, Nübel V, Preusch K, Bruhns OT. High order finite elements for shells. Comput Methods Appl Mech Eng 2005;194(21-24):2494–512.
[4] Ribeiro P. Forced periodic vibrations of laminated composite plates by a p-version, first order shear deformation, finite element. Composit Sci Technol 2006;66(11-12):1844–56.
[5] Houmat A. Three-dimensional free vibration analysis of plates using the hp-version of the finite element method. J Sound Vibr 2006;290(3-5):690–704.
[6] Hughes TJ, Cottrell JA, Bazilevs Y. Isogeometric analysis: CAD, finite elements, NURBS, exact geometry and mesh refinement. Comput Methods Appl Mech Eng 2005;194(39-41):4135–95.
[7] Tin-Loi F, Ngo NS. Performance of a p-adaptive finite element method for shakedown analysis. Int J Mech Sci 2007;49(10):1166–78.
[8] Khoei AR, Azadi H, Moslemi H. Modeling of crack propagation via an automatic adaptive mesh refinement based on modified superconvergent patch recovery technique. Engineering Fracture Mechanics 2008;75(10):2921–45.
[9] Park K, Paulino GH, Celes W, Espinha R. Adaptive mesh refinement and coarsening for cohesive zone modeling of dynamic fracture. Int J Numer Methods Eng 2012;92(1):1–35.
[10] Soghrati S, Nagarajan A, Liang B. Conforming to interface structured adaptive mesh refinement: new technique for the automated modeling of materials with complex microstructures. Finite Elements Anal Des 2017;125:24–40.
[11] Jaccon A, Prabel B, Molnár G, Bluthé J, Gravouil A. Adaptive mesh refinement and cycle jumps for phase-field fatigue fracture modeling. Finite Elements Anal Design 2023;224:104004.
[12] Wang C, Ping X, Wang X. An adaptive finite element method for crack propagation based on a multifunctional super singular element. Int J Mech Sci 2023;247(108191).
[13] Eibner T, Melenk JM. An adaptive strategy for hp-FEM based on testing for analyticity. Comput Mech 2007;39:575–95.
[14] Zboinski G. Adaptive hpq finite element methods for the analysis of 3D-based models of complex structures. Part 2. a posteriori error estimation. Comput Methods Appl Mech Eng 2013;267:531–65.
[15] Daniel P, Ern A, Smears I, Vohralík M. An adaptive hp-refinement strategy with computable guaranteed bound on the error reduction factor. Comput Math Appl 2018;76(5):967–83.
[16] Bird RE, Augarde CE, Coombs WM, Duddu R, Giani S, Huynh PT, et al. An hp-adaptive discontinuous Galerkin method for phase field fracture. Comput Methods Appl Mech Eng 2023;416(116336).
[17] Park JW, Hwang JW, Kim YH. Efficient finite element analysis using mesh superposition technique. Finite Elem Anal Des 2003;39(7):619–38.
[18] Krause R, Rank E. Multiscale computations with a combination of the h- and p-versions of the finite-element method. Comput Methods Appl Mech Eng 2003;192(35-36):3959–83.
[19] Sun W, Fish J, Dhia HB. A variant of the s-version of the finite element method for concurrent multiscale coupling. Int J Multiscale Comput Eng 2018;16(2).
[20] Nakasumi S, Suzuki K, Ohtsubo H. Crack growth analysis using mesh superposition technique and X-FEM. Int J Numer Methods Eng 2008;75(3):291–304.
[21] Zander ND. Multi-level hp-FEM: dynamically changing high-order mesh refinement with arbitrary hanging nodes [Ph.D. Thesis], Technische Universität München; 2017.
[22] Kishi K, Takeoka Y, Fukui T, Matsumoto T, Suzuki K, Shibanuma K. Dynamic crack propagation analysis based on the s-version of the finite element method. Comput Methods Appl Mech Engrg 2020;366(113091).
[23] Xu Q, Chen J, Yue H, Li J. A study on the S-version FEM for a dynamic damage model. Int J Numerical Methods Eng 2018;115(4):427–44.
[24] Sakata S, Chan Y, Arai Y. On accuracy improvement of microscopic stress/stress sensitivity analysis with the mesh superposition method for heterogeneous materials considering geometrical variation of inclusions. Int J Numer Methods Eng 2020;121(3):534–59.
[25] Wagner W. A path-following algorithm with quadratic predictor. Comput Struct 1991;39(3–4):339–48.
[26] Cadou JM, Damil N, Potier-Ferry M, Braikat B. Projection techniques to improve high-order iterative correctors. Finite Elem Anal Des 2004;41(3):285–309.
[27] Eriksson A, Kouhia R. On step size adjustments in structural continuation problems. Comput Struct 1995;55(3):495–506.
[28] Cadou JM, Duigou L, Damil N, Potier-Ferry M. Convergence acceleration of iterative algorithms. Applications to thin shell analysis and Navier–Stokes equations. Comput Mech 2009;43:253–64.
[29] Riks E. The application of Newton's method to the problem of elastic stability. J Appl Mech 1972;39(4):1060–5.
[30] Ramm E. Strategies for tracing the nonlinear response near limit points. In: Nonlinear finite element analysis in structural mechanics: proceedings of the Europe-US workshop Ruhr-universität. Bochum, Germany; p. 63–89.
[31] Crisfield MA. A fast incremental/iterative solution procedure that handles "snap-through". Comput Struct 1981;13(1):55–62.
[32] Koiter WT. On the stability of elastic equilibrium [Ph.D. thesis], TU-Delft; 1967.
[33] Thompson JMT, Walker AC. The non-linear perturbation analysis of discrete structural systems. Int J Solids Struct 1968;4(8):757–68.
[34] Gallagher RH. Perturbation procedures in nonlinear finite element structural analysis. In: Computational mechanics – lecture notes in mathematics, vol. 461, 1975, p. 75–89.
[35] Noor AK. Recent advances in reduction methods for nonlinear problems. Comput Methods Nonlinear Struct Solid Mech 1981;13:31–44.
[36] Riks E. Some computational aspects of the stability analysis of nonlinear structures. Comput Methods Appl Mech Engrg 1984;47(3):219–59.
[37] Lanzo AD, Garcea G, Casciaro R. Asymptotic post-buckling analysis of rectangular plates by HC finite elements. Internat J Numer Methods Engrg 1995;38(14):2325–45.
[38] Jansen EL. A perturbation method for nonlinear vibrations of imperfect structures: application to cylindrical shell vibrations. Int J Solids Struct 2008;45(3–4):1124–45.
[39] Shen HS. Postbuckling of shear deformable FGM cylindrical shells surrounded by an elastic medium. Int J Mech Sci 2009;51(5):372–83.
[40] Garcea G, Liguori FS, Leonetti L, Magisano D, Madeo A. Accurate and efficient a posteriori account of geometrical imperfections in koiter finite element analysis. Internat J Numer Methods Engrg 2017;112(9):1154–74.
[41] Madeo A, Groh RMJ, Zucco G, Weaver PM, Zagari G, Zinno R. Post-buckling analysis of variable-angle tow composite plates using Koiter's approach and the finite element method. Thin-Walled Struct 2017;110:1–13.
[42] Vescovini R, Spigarolo E, Jansen EL, Dozio L. Efficient post-buckling analysis of variable-stiffness plates using a perturbation approach. Thin-Walled Struct 2019;143(106211).
[43] Li ZM, Liu T, Qiao P. Buckling and postbuckling of anisotropic laminated doubly curved panels under lateral pressure. Int J Mech Sci 2021;206(106615).
[44] Damil N, Potier-Ferry M. A new method to compute perturbed bifurcations: application to the buckling of imperfect elastic structures. Internat J Engrg Sci 1990;28(9):943–57.
[45] Azrar L, Cochelin B, Damil N, Potier-Ferry M. An asymptotic-numerical method to compute the postbuckling behaviour of elastic plates and shells. Internat J Numer Methods Engrg 1993;36(8):1251–77.
[46] Cochelin B, Damil N, Potier-Ferry M. The asymptotic-numerical method: an efficient perturbation technique for nonlinear structural mechanics. Eur J Comput Mech 1994;3(2):281–97.
[47] Cochelin B. A path-following technique via an asymptotic-numerical method. Comput Struct 1994;53(5):1181–92.
[48] Potier-Ferry M, Cadou JM. Basic ANM algorithms for path following problems. Rev Eur Eléments Finis 2004;13(1–2):9–32.
[49] Elhage-Hussein A, Potier-Ferry M, Damil N. A numerical continuation method based on padé approximants. Int J Solids Struct 2000;37(46–47):6981–7001.
[50] Vannucci P, Cochelin B, Damil N, Potier-Ferry M. An asymptotic-numerical method to compute bifurcating branches. Internat J Numer Methods Engrg 1998;41(8):1365–89.

[51] Najah A, Cochelin B, Damil N, Potier-Ferry M. A critical review of asymptotic numerical methods. Arch Comput Methods Eng 1998;5(1):31–50.
[52] Zahrouni H, Cochelin B, Potier-Ferry M. Computing finite rotations of shells by an asymptotic-numerical method. Comput Methods Appl Mech Engrg 1999;175(1–2):71–85.
[53] Cochelin B, Compain C. An asymptotic numerical method for non-linear transient dynamics. Rev Eur Eléments Finis 2000;9(1–3):113–28.
[54] Azrar L, Benamar R, Potier-Ferry M. An asymptotic-numerical method for large-amplitude free vibrations of thin elastic plates. J Sound Vib 1999;220(4):695–727.
[55] Azrar L, Boutyour EH, Potier-Ferry M. Non-linear forced vibrations of plates by an asymptotic–numerical method. J Sound Vib 2002;252(4):657–67.
[56] Givois A, Grolet A, Thomas O, Deü JF. On the frequency response computation of geometrically nonlinear flat structures using reduced-order finite element models. Nonlinear Dynam 2019;97(2):1747–81.
[57] Bilasse M, Azrar L, Daya EM. Complex modes based numerical analysis of viscoelastic sandwich plates vibrations. Comput Struct 2011;89(7–8):539–55.
[58] Boumédiène F, Duigou L, Boutyour EH, Miloudi A, Cadou JM. Nonlinear forced vibration of damped plates coupling asymptotic numerical method and reduction models. Comput Mech 2011;47:359–77.
[59] Yu K, Hu H, Tang H, Giunta G, Potier-Ferry M, Belouettar S. A novel two-dimensional finite element to study the instability phenomena of sandwich plates. Comput Methods Appl Mech Engrg 2015;283:1117–37.
[60] Abdelkhalek S, Zahrouni H, Legrand N, Potier-Ferry M. Post-buckling modeling for strips under tension and residual stresses using asymptotic numerical method. Int J Mech Sci 2015;104:126–37.
[61] Raju G, Wu Z, White S, Weaver PM. Optimal postbuckling design of variable angle tow composite plates. AIAA J 2018;56(5):2045–61.
[62] Yan CA, Vescovini R. Application of the ps-version of the finite element method to the analysis of laminated shells. Materials 2023;16(4):1395.
[63] Baker GA, Graves-Morris P. Padé approximants. Part 1: Basic theory. Encyclopedia of Mathematics and its Applications; 1981.
[64] Cochelin B, Damil N, Potier-Ferry M. Asymptotic–numerical methods and padé approximants for non-linear elastic structures. Internat J Numer Methods Engrg 1994;37(7):1187–213.
[65] Mote Jr CD. Global-local finite element. Internat J Numer Methods Engrg 1971;3(4):565–74.
[66] Fish J. The s-version of the finite element method. Comput Struct 1992;43(3):539–47.
[67] Zander N, Bog T, Elhaddad M, Frischmann F, Kollmannsberger S, Rank E. The multi-level hp-method for three-dimensional problems: Dynamically changing high-order mesh refinement with arbitrary hanging nodes. Comput Methods Appl Mech Engrg 2016;310:252–77.
[68] Babuška I, Rank E. An expert-system-like feedback approach in the hp-version of the finite element method. Finite Element Anal 1987;3(2):127–47.
[69] Bern M, Flaherty J, Luskin M. Grid generation and adaptive algorithms. New York, NY, USA: Springer Science & Business Media; 2012.
[70] Hao P, Liao H, Wu T, Huo Z, Wang B. Isogeometric degenerated shell formulation for post-buckling analysis of composite variable-stiffness shells. Compos Struct 2023;321(117209).
[71] Li DM, Featherston CA, Wu Z. An element-free study of variable stiffness composite plates with cutouts for enhanced buckling and post-buckling performance. Comput Methods Appl Mech Engrg 2020;371(113314).
[72] Arbocz J, Starnes JH. On a high-fidelity hierarchical approach to buckling load calculations. New Approach Struct Mech Shells Biol Struct 2002;271–92.
[73] Rahman T, Jansen EL. Finite element based coupled mode initial post-buckling analysis of a composite cylindrical shell. Thin-Walled Struct 2010;48(1):25–32.
[74] Notenboom R, Jansen EL. Modal interaction studies in cylindrical shell buckling through advanced multimode analysis tools. In: AIAA sciTech forum. 2022, p. 1491.
[75] Wu Z, Raju G, Weaver PM. Comparison of variational, differential quadrature, and approximate closed-form solution methods for buckling of highly flexurally anisotropic laminates. J Eng Mech 2012;139(8):1073–83.
[76] Vescovini R, Dozio L, D'Ottavio M, Polit O. On the application of the ritz method to free vibration and buckling analysis of highly anisotropic plates. Compos Struct 2018;192:460–74.
[77] Castro SG, Mittelstedt C, Monteiro FA, Arbelo MA, Degenhardt R, Ziegmann G. A semi-analytical approach for linear and non-linear analysis of unstiffened laminated composite cylinders and cones under axial, torsion and pressure loads. Thin-Walled Struct 2015;90:61–73.
[78] Gürdal Z, Olmedo R. Composite laminates with spatially varying fiber orientations: Variable stiffness panel concept. In: 33rd AIAA/aSME/ASCE/AHS/aSC structures, structural dynamics and material conference. 1992.
[79] Wu Z, Weaver PM, Raju G. Postbuckling optimisation of variable angle tow composite plates. Compos Struct 103:1032013, 34–42.
[80] Pagani A, Azzara R, Carrera E. Geometrically nonlinear analysis and vibration of in-plane-loaded variable angle tow composite plates and shells. Acta Mech 2022;1–24.